



Comparison of airborne measurements of NO, NO₂, HONO, NO_y and CO during FIREX-AQ

Ilann Bourgeois^{1,2,*}, Jeff Peischl^{1,2,*}, J. Andrew Neuman^{1,2}, Steven S. Brown^{2,3}, Hannah M. Allen⁴, Pedro Campuzano-Jost^{1,3}, Matthew M. Coggon^{1,2}, Joshua P. DiGangi⁵, Glenn S. Diskin⁵, Jessica B. Gilman², Georgios I. Gkatzelis^{1,2,a}, Hongyu Guo^{1,3}, Hannah A. Halliday^{5,b}, Thomas F. Hanisco⁶, Christopher D. Holmes⁷, L. Gregory Huey⁸, Jose L. Jimenez^{1,3}, Aaron D. Lamplugh^{1,2}, Young Ro Lee⁸, Jakob Lindaas⁹, Richard H. Moore⁵, John B. Nowak⁵, Demetrios Pagonis^{1,3,c}, Pamela S. Rickly^{1,2}, Michael A. Robinson^{1,2,3}, Andrew W. Rollins², Vanessa Selimovic¹⁰, Jason M. St. Clair^{7,11}, David Tanner⁸, Krystal T. Vasquez⁴, Patrick R. Veres², Carsten Warneke², Paul O. Wennberg^{12,13}, Rebecca A. Washenfelder², Elizabeth B. Wiggins⁵, Caroline C. Womack^{1,2}, Lu Xu^{12,d}, Kyle J. Zarzana^{1,2,e} and Thomas B. Ryerson^{2,f}

¹Cooperative Institute for Research in Environmental Sciences, University of Colorado Boulder, Boulder, CO, USA

²NOAA Chemical Sciences Laboratory (CSL), Boulder, CO, USA

³Department of Chemistry, University of Colorado Boulder, Boulder, CO, USA

⁴Division of Chemistry and Chemical Engineering, California Institute of Technology, Pasadena, CA, USA

⁵NASA Langley Research Center, Hampton, VA, USA

⁶Atmospheric Chemistry and Dynamics Laboratory, NASA Goddard Space Flight Center, Greenbelt, MD, USA

⁷Department of Earth, Ocean and Atmospheric Science, Florida State University, Tallahassee, FL, USA

⁸School of Earth and Atmospheric Sciences, Georgia Institute of Technology, Atlanta, GA, USA

⁹Department of Atmospheric Science, Colorado State University, Fort Collins, CO, USA

¹⁰Department of Chemistry and Biochemistry, University of Montana, Missoula, MT, USA

¹¹Joint Center for Earth Systems Technology, University of Maryland Baltimore County, Baltimore, MD, USA

¹²Division of Geological and Planetary Sciences, California Institute of Technology, Pasadena, CA, USA

¹³Division of Engineering and Applied Science, California Institute of Technology, Pasadena, CA, USA

^anow at Institute of Energy and Climate Research, IEK-8: Troposphere, Forschungszentrum Jülich GmbH, Jülich, Germany

^bnow at Office of Research and Development, US EPA, Research Triangle Park, NC, USA

^cnow at Department of Chemistry and Biochemistry, Weber State University, Ogden, UT, USA

^dnow at 1 and 2

^enow at 3

^fnow at Scientific Aviation, Boulder, CO, USA

*corresponding authors: Ilann Bourgeois (ilann.bourgeois@colorado.edu)/Jeff Peischl (jeff.peischl@noaa.gov)



Abstract

1 We present a comparison of fast-response instruments installed onboard the NASA DC-8
2 aircraft that measured nitrogen oxides (NO and NO₂), nitrous acid (HONO), total reactive
3 odd nitrogen (measured both as the total (NO_y) and from the sum of individually measured
4 species (ΣNO_y)) and carbon monoxide (CO) in the troposphere during the 2019 Fire
5 Influence on Regional to Global Environments and Air Quality (FIREX-AQ) campaign. By
6 targeting smoke from summertime wildfires, prescribed fires and agricultural burns across
7 the continental United States, FIREX-AQ provided a unique opportunity to investigate
8 measurement accuracy in concentrated plumes where hundreds of species coexist. Here, we
9 compare NO measurements by chemiluminescence (CL) and laser induced fluorescence
10 (LIF); NO₂ measurements by CL, LIF and cavity enhanced spectroscopy (CES); HONO
11 measurements by CES and iodide-adduct chemical ionization mass spectrometry (CIMS);
12 and CO measurements by tunable diode laser absorption spectrometry (TDLAS) and
13 integrated cavity output spectroscopy (ICOS). Additionally, total NO_y measurements using
14 the CL instrument were compared with ΣNO_y (= NO + NO₂ + HONO + nitric acid (HNO₃) +
15 acyl peroxy nitrates (APNs) + submicron particulate nitrate (pNO₃)). The aircraft instrument
16 intercomparisons demonstrate the following: 1) NO measurements by CL and LIF agreed
17 well within instrument uncertainties, but with potentially reduced time response for the CL
18 instrument; 2) NO₂ measurements by LIF and CES agreed well within instrument
19 uncertainties, but CL NO₂ was on average 10% higher; 3) CES and CIMS HONO
20 measurements were highly correlated in each fire plume transect, but the correlation slope of
21 CES vs. CIMS for all 1 Hz data during FIREX-AQ was 1.8, which we attribute to a reduction
22 in the CIMS sensitivity to HONO in high temperature environments; 4) NO_y budget closure
23 was demonstrated for all flights within the combined instrument uncertainties of 25%.
24 However, we used a fluid dynamic flow model to estimate that average pNO₃ sampling
25 fraction through the NO_y inlet in smoke was variable from one flight to another and ranged
26 between 0.36 and 0.99, meaning that approximately 0–24% on average of the total measured
27 NO_y in smoke may have been unaccounted for and may be due to unmeasured species such
28 as organic nitrates; 5) CO measurements by ICOS and TDLAS agreed well within combined
29 instrument uncertainties, but with a systematic offset that averaged 2.87 ppbv; and 6)
30 integrating smoke plumes followed by fitting the integrated values of each plume improved
31 the correlation between independent measurements.



32 **1. Introduction**

33 Biomass burning (BB) can take multiple forms (e.g., wildfires, prescribed fires, agricultural
34 burns, grass fires, peat fires) and accounts for a large fraction of global carbon emissions with
35 consequences for climate (Bowman et al., 2009; van der Werf et al., 2010, 2017) and
36 biogeochemical cycles (Crutzen & Andreae, 2016). BB also contributes substantially to the
37 atmospheric burden of trace gases and aerosols (Andreae, 2019), causing poor air quality on
38 regional to continental scales (Jaffe et al., 2020; O'Dell et al., 2019; Wotawa, 2000) and
39 posing a major threat to public health (Johnston et al., 2012, 2021). In the United States (US),
40 wildfires mainly occur in the western states and in Alaska and burned over 4.5 million acres
41 in 2019 (US National Interagency Fire Center, <https://www.nifc.gov/fire-information>).
42 Wildfires frequency and severity are predicted to increase in response to a warmer, drier
43 climate (Burke et al., 2021; Westerling, 2016) and also to increasing human-caused ignition
44 (Balch et al., 2017). In comparison, prescribed fires, which are common practice in the
45 southeastern US, burned an estimated 10 million acres in 2019, to which agricultural burns
46 added another 2–3 million acres (Melvin, 2020). While agricultural burns are usually smaller
47 and less intense than wildfires or prescribed fires, they occur more frequently and throughout
48 the whole year, and can significantly impact local air quality (Dennis et al., 2002; McCarty,
49 2011).

50
51 Rising interest in the impact of fires on climate and air quality over the past decades has
52 resulted in a series of laboratory studies of BB emissions in the US such as the FLAME-4
53 experiment in 2012 (e.g., Stockwell et al., 2014) and the FIRELAB study in 2016 (e.g.,
54 Selimovic et al., 2018). Recent, large-scale field studies such as AMMA (e.g., Liousse et al.,
55 2010), BBOP (e.g., Collier et al., 2016) and WE-CAN (e.g., Calahorrano et al., 2020) have
56 been dedicated to sampling and characterizing emissions and atmospheric chemistry from
57 fires. The focus of the joint National Oceanic and Atmospheric Administration (NOAA) /
58 National Aeronautics and Space Administration (NASA) Fire Influence on Regional to
59 Global Environments and Air Quality (FIREX-AQ) airborne campaign was to provide
60 comprehensive observations to investigate the impact of summer time wildfires, prescribed
61 fires and agricultural burns on air quality and climate across the conterminous US.
62 Accurate measurements facilitate understanding of fire emissions, processing and impacts. In
63 situ, fast-response measurements of trace gases in the atmosphere conducted from airborne
64 platforms provide unique data sets that enhance our understanding of atmospheric
65 composition and chemistry. One method for evaluating measurement accuracy is by
66 comparison of independent measurements using different techniques. A relatively small body
67 of literature reported comparisons of methods for in flight detection of tropospheric carbon
68 monoxide (CO) and reactive odd nitrogen species measured both as the total (NO_y) and from
69 the sum of individually measured species (ΣNO_y), and these studies have shown that such
70 comparisons are valuable for identifying instrument artifacts and quantifying measurement
71 uncertainties (Eisele et al., 2003; Gregory et al., 1990; Hoell et al., 1987; Hoell et al., 1987;
72 Sparks et al., 2019). During FIREX-AQ, a large suite of airborne instruments, detailed in the
73 following sections, performed independent in situ tropospheric measurements of one or more
74 fire-science relevant reactive nitrogen species and CO aboard the NASA DC-8 aircraft.



75 Additionally, FIREX-AQ provides a unique opportunity to investigate measurement accuracy
76 in concentrated smoke plumes where hundreds of species coexist.

77

78 Nitric oxide (NO) and nitrogen dioxide (NO₂) are among the largest components of the
79 reactive nitrogen budget emitted by biomass burning and are produced by the oxidation of
80 reduced nitrogen species present in the fuel in the flaming stage of combustion (Roberts et
81 al., 2020). NO_x, defined as the sum of NO and NO₂, directly affects atmospheric oxidation
82 rates and ozone (O₃) production within fire plumes (Robinson et al., 2021; L. Xu et al.,
83 2021). It also contributes to the formation of secondary aerosols and N transport and
84 deposition to ecosystems downwind (Galloway et al., 2003; Kroll & Seinfeld, 2008; Ziemann
85 & Atkinson, 2012). Therefore, two independent NO and three independent NO₂
86 measurements were part of FIREX-AQ to provide continuous in situ observations, as
87 described in section 2 below. Nitrous acid (HONO) is emitted directly to the atmosphere
88 through various combustion processes including BB. The rapid production of OH from
89 HONO at the early stage of smoke plume formation (Peng et al., 2020) results in rapid
90 initiation of photochemistry, with a strong influence on downwind chemical evolution of
91 smoke plumes (Robinson et al., 2021; Theys et al., 2020). Total NO_y can be measured
92 through conversion of individual species to NO (Fahey et al., 1985). It is a more conserved
93 tracer for NO_x emissions than NO_x itself since it accounts for NO_x oxidation products, and it
94 provides a mean to assess from a mass-balance approach the accuracy of ΣNO_y budget
95 closure (Bollinger et al., 1983; Fahey et al., 1986; Williams et al., 1997). ΣNO_y usually
96 consists of NO_x, HONO, nitric acid (HNO₃), nitrogen pentoxide (N₂O₅), peroxyxynitric acid
97 (HNO₄), acyl peroxy nitrates (APNs), halogen-nitrogen species such as ClNO₂, other organic
98 nitrates such as alkyl nitrates, and particulate nitrate (pNO₃). Carbon monoxide (CO) is
99 emitted from incomplete combustion in fires and other sources, and is especially important
100 for characterizing the combustion stage of fires (i.e., flaming vs. smoldering) through the use
101 of the modified combustion efficiency (Yokelson et al., 1996). Due to its relatively long
102 chemical lifetime, CO is commonly used as a conserved tracer to account for dilution with
103 ambient air as smoke plumes are transported downwind, and accurate CO measurements are
104 necessary to better constrain emission factors (EFs) used in emission inventories.

105

106 This study builds on past airborne instrument comparisons and extends these analyses to a
107 new species (HONO), new measurement techniques (first airborne deployment of the NOAA
108 NO-LIF (laser induced fluorescence) and the NOAA CO-ICOS (integrated cavity output
109 spectroscopy) instruments) and new environments (concentrated fire smoke). In this paper we
110 present a comparison of NO, NO₂, HONO, NO_y and CO measurements, which are
111 compounds of major interest for fire-related science, air quality and climate. In the first part
112 of this paper, we describe the FIREX-AQ campaign, the deployed instruments and the
113 methodology used to perform the comparisons. In the second part, we provide a detailed
114 instrument comparison for each species.

115

116 2. FIREX-AQ overview and instruments

117 2.1 FIREX-AQ airborne mission



118 The FIREX-AQ campaign (<https://www-air.larc.nasa.gov/missions/firex-aq/>;
119 <https://www.esrl.noaa.gov/csl/projects/firex-aq/>) took place from July to September 2019.
120 FIREX-AQ included the deployment of multiple aircraft and mobile platforms over the
121 course of the campaign, however this study focuses on the heavily instrumented NASA DC-8
122 aircraft. The NASA DC-8 portion of the project achieved two flights over the Los Angeles
123 (LA) Basin and the Central Valley in California, 13 flights originating from Boise, Idaho, and
124 7 flights based out of Salina, Kansas. The flights from Boise were conducted over the
125 Western US to sample smoke from wildfires, while the flights from Salina focused on
126 agricultural and prescribed burns (hereafter referred to as eastern fires) in the Southeastern
127 US.

128
129 Most wildfire flights were designed to sample background mixing ratios, fresh emissions, and
130 aged smoke, whereas the eastern fire flights typically transected numerous fresh smoke
131 plumes several times each. For wildfires, the NASA DC-8 first flew upwind of the fire to
132 characterize ambient conditions unaffected by targeted fire emissions. Subsequent cross-wind
133 plume transects were conducted as close as possible to the fire to sample the emissions with
134 the minimal atmospheric ageing. Plume transects were designed to be perpendicular to the
135 wind direction and through the center of the vertical extent of the plume, terrain permitting.
136 The vertical structure of the plume was systematically assessed using a differential absorption
137 lidar during a lengthwise overpass above the plume from end to start. The aircraft transected
138 the smoke plume successively further downwind, at approximately 15–40 km intervals, to
139 characterize smoke evolution in a “lawnmower” pattern (Figure 1a). For several wildfires, the
140 DC-8 also executed flight transects along the plume axis, both toward and away from the fire
141 source. Most eastern fires sampled during FIREX-AQ did not produce plumes large enough
142 to enable regularly spaced plume transects. Most smoke plumes were therefore sampled
143 repetitively at the same location, sometimes with varying altitude and/or approach angle
144 (Figure 1b).

146 2.2 Instruments

147 2.2.1 Chemiluminescence (NO/NO₂/NO_y)

148 The NOAA CL instrument has been frequently used for both ground-based and airborne
149 measurements of NO, NO₂ and NO_y and uses the CL detection of NO with O₃ added as
150 reagent gas (Fontijn et al., 1970; Ridley & Grahek, 1990; Ridley & Howlett, 1974; Ryerson
151 et al., 1999, 2000). NO, NO₂ and NO_y are measured on three independent channels of the
152 instrument. The NO channel measures NO, the NO₂ channel measures the sum of NO and
153 photolyzed NO₂ as NO, and the NO_y channel measures the total reactive nitrogen oxides
154 species reduced to NO. NO₂ is determined from the difference between signals from the NO
155 and NO₂ channels. Ambient air is continuously sampled from a pressure-building ducted
156 aircraft inlet to the instrument at a typical flow of 1045.1 ± 0.2, 1030.2 ± 0.2 and 1029.5 ±
157 0.2 standard cubic centimeters per minute (sccm) in flight for NO, NO₂, and NO_y,
158 respectively. In the NO₂ channel, NO₂ is photolyzed to NO using ultraviolet (UV) LEDs at
159 385 nm in a 45 cm long quartz cell (inner diameter of 1.2 cm) pressure-controlled at 209.8 ±
160 0.3 Torr (Pollack et al., 2011). In the NO channel, a similar quartz cell wrapped in aluminum
161 foil to avoid NO₂ photolysis and pressure controlled at 209.7 ± 0.3 Torr, ensures similar



162 residence time of sampled air in both channels. In the NO_y channel, reactive odd nitrogen
163 species are first sampled through an inlet heated at $90.0 \pm 0.1^\circ\text{C}$ then catalytically reduced to
164 NO on a gold tube surface heated at $300.0 \pm 0.2^\circ\text{C}$ in the presence of added pure CO flowing
165 at 3.19 ± 0.01 sccm. Approximately 5% O_3 in oxygen is produced by corona discharge,
166 delivered at 73.80 ± 0.02 (NO channel), 74.11 ± 0.03 (NO_2 channel), and 74.60 ± 0.04 (NO_y
167 channel) sccm, and mixed with sampled air in a pressure (8.65 ± 0.02 , 8.79 ± 0.02 , $8.56 \pm$
168 0.02 Torr for NO, NO_2 , and NO_y respectively) and temperature (25.0 ± 0.2 and 25.1 ± 0.2
169 and $25.1 \pm 0.2^\circ\text{C}$ for NO and NO_2 , respectively) controlled reaction vessel. O_3 -induced CL is
170 detected with a red-sensitive photomultiplier tube controlled at -78°C with dry ice, and the
171 amplified digitized signal is recorded using an 80 MHz counter. Pulse coincidence at high
172 count rates was calculated after the mission by fitting an inverse function to the curve
173 between observed and theoretical count rates for known NO mixing ratios ranging from ppbv
174 to ppmv levels. Instrument calibrations were routinely performed both on the ground and
175 during flight by standard addition of NO from a gravimetrically determined NO in N_2
176 mixture (1.38 ± 0.03 ppmv) delivered at 4.04 ± 0.02 (NO channel), 4.84 ± 0.02 (NO_2
177 channel), and 4.96 ± 0.02 (NO_y channel) sccm. All measurements were taken at a temporal
178 resolution of 0.1 second (s), averaged to 1 s, and corrected for the dependence of instrument
179 sensitivity on ambient water vapor content (Ridley et al., 1992). Finally, NO_2 data were
180 further corrected for a 5% HONO interference due to HONO photolysis at 385 nm quantified
181 from theoretical calculation and confirmed in the laboratory using a HONO source described
182 in Lao et al. (2020). Under these conditions the total estimated 1Hz uncertainty at sea level
183 was $\pm (4\% + 6 \text{ pptv})$, $\pm (7\% + 20 \text{ pptv})$, and $\pm (12\% + 15 \text{ pptv})$ for NO, NO_2 , and NO_y ,
184 respectively.

185

186 2.2.2 Laser Induced Fluorescence (NO)

187 The NOAA NO-LIF measurements were performed using a custom-built laser-induced
188 fluorescence instrument as detailed in Rollins et al. (2020). Air was continuously sampled
189 from outside the aircraft through an optical cell in the DC-8 cabin held to near 90 hPa. The
190 instrument utilizes a fiber laser system with a narrow-band laser tuned to a rotationally
191 resolved NO spectral feature near 215 nm. Rapid dithering on and off of this resonance
192 achieves 0.1 s measurements with a continuously monitored background to reduce
193 uncertainty in the instrument zero. The laser induced excitation of NO is followed by red-
194 shifted fluorescence which is detected by a photomultiplier tube operated in single-photon
195 counting mode. The laser is directed through both a sampling and reference cell in a single
196 pass for continuous monitoring of any changes in the instrument sensitivity due to changes in
197 the laser spectrum, or pressure of the optical cells. 500 ppbv of NO in air was flown at 50
198 sccm through the reference cell to ensure that measurements are occurring with the laser
199 tuned to the peak online wavelength. A constant flow of approximately 2500 sccm is
200 maintained within the sampling cell through the use of a custom inlet valve (Gao et al., 1999)
201 and the exhaust of both cells are tied together allowing for any changes in sensitivity due to
202 pressure fluctuations to be accounted for during data reduction. Hourly calibrations were
203 performed during each flight in which 2–10 sccm of 5 ppmv NO in N_2 mixture was added to
204 the sample flow resulting in mixing ratios of 4–20 ppbv. The sensitivity of the instrument
205 was determined using the in-flight calibrations to be typically 10 counts per second (CPS)



206 pptv⁻¹ with 10 CPS background achieving a detection limit of 1 pptv for 1 s integration. The
207 uncertainty of the instrument sensitivity is $\pm 6\text{--}9\%$. The effect of water vapor, which reduces
208 the sensitivity by quenching of the electronically excited NO, was accounted for during data
209 reduction using water vapor measurements provided by an ICOS instrument on the DC-8.

210

211 2.2.3 Laser Induced Fluorescence (NO₂)

212 The NASA Compact Airborne NO₂ Experiment (CANOE) measured NO₂ using non-resonant
213 LIF. The instrument is a modified version of a formaldehyde (HCHO) instrument (St. Clair et
214 al., 2019) with the excitation wavelength changed to 532 nm. The technique utilizes the
215 pulsed (80 kHz) output of a fixed wavelength, 2W, 532 nm laser to excite NO₂ molecules and
216 detects the resulting fluorescence with two identical detection axes consisting of a
217 photomultiplier tube (PMT) and optical filters that transmit > 695 nm. Delayed time gate
218 PMT counts are recorded at 10 Hz and a laboratory calibration, along with an intercept
219 determined by preflight zeroing, are used to provide 1Hz NO₂ data. The NO₂ measurement
220 uncertainty is estimated to be $\pm (10\% + 100$ pptv).

221

222 During FIREX-AQ, ambient air was sampled using a shared inlet that provided a large (10–
223 25 standard liter per minute (slpm)) bypass flow to the instrument rack. The CANOE
224 instrument pulled its 750 sccm sample flow from a shared manifold at the instrument rack.
225 An inline particle filter on the sample line prevented laser scatter by fine aerosol that were
226 not removed by the particle-rejecting inlet. A manual three-way valve outside the instrument
227 was used to sample from a scrubber (Drierite/molecular sieve) and provide a zero before and
228 periodically during the flight. Pressure in the CANOE detection cell was maintained at 40
229 Torr by a pressure controller that precedes the cell in the flow path.

230

231 2.2.4 Cavity Enhanced Spectroscopy (NO₂/HONO)

232

233 NO₂ and HONO were also measured by the NOAA airborne cavity enhanced spectroscopy
234 (ACES) instrument. This technique is based on incoherent broadband cavity enhanced
235 spectroscopy (CES, Fiedler et al., 2003). The CES instrument is described in full detail by
236 Min et al. (2016) with only minor changes for FIREX-AQ. Briefly, the system consists of
237 two parallel 45 cm optical cavities capped by highly reflective mirrors, with reflectivity
238 curves centered at 365 nm ($R = 0.99987$) and 455 nm ($R = 0.99992$). Each cavity is
239 illuminated by a broadband LED light source (centered at 365 and 455 nm respectively)
240 collimated by an off-axis parabola, and passively coupled into the cavity. The light makes
241 many passes before exiting the cavity into a fiber optic cable, which transmits the light to a
242 grating spectrometer spanning 350–475 nm. The LEDs are modulated on for 0.4 s and off for
243 0.08 s for charged-couple device (CCD) readout, giving a total integration time of 0.48 s per
244 light intensity spectrum. An absorption spectrum of the ambient air sample is determined
245 using the procedure presented by Washenfelder et al. (2008). The procedure requires
246 comparing the measured light intensity spectrum to a background spectrum of the cavity
247 filled with zero air, which is determined here every 10 minutes. The mirror reflectivity is
248 measured every hour using the Rayleigh scattering difference between helium and zero air,
249 and the spectrometer dark counts and wavelength calibration are measured every two hours.



250 A small flow from a mixture of 25 ppm NO₂ in air is diluted into the cavity every hour,
251 resulting in NO₂ concentrations between 50 and 100 ppbv, to assess the NO₂ spectral retrieval
252 features on the spectrometer. The absolute concentration was not used for calibration of the
253 NO₂ response, but rather for providing a reference NO₂ spectrum. Glyoxal reference spectra
254 was obtained by bubbling zero air through a Teflon bubbler with 40% glyoxal in water as in
255 Min et al. (2016).

256
257 Ambient air is pulled through the inlet into the two optical cavities at a flow rate of 5.4
258 volumetric liters per minute per cavity by a scroll pump. The air passes through two 1 μm
259 pore size Teflon filters before entering the instrument to remove any aerosol particles. Mirror
260 cleanliness is maintained by flowing 150 sccm zero air over each mirror to prevent
261 condensation of semi-volatile species. A pressure controller consisting of a Teflon orifice and
262 a variable flow to a bypass maintains the internal pressure at one of two pressure set points:
263 400 mbar when the aircraft was below 7.3 km, and 150 mbar above 7.3 km. The residence
264 time of the air inside the optical cavities is estimated to be 0.5 s.

265
266 The measured absorption spectrum is fit to a linear combination of literature or reference
267 spectra of absorbing gas-phase species and a polynomial to account for drifts in the cavity
268 stability or light source intensity, as detailed by Min et al. (2016), using a Levenberg-
269 Marquardt least-squares fitting algorithm. For the 365 nm channel, those species are NO₂,
270 HONO, O₄, and a 4th order polynomial. For the 455 nm channel, those species are NO₂,
271 glyoxal, methylglyoxal, H₂O, and O₄, as well as a 0th order polynomial, though only NO₂ is
272 presented here. The algorithm uses reference spectra for NO₂ and glyoxal, as measured in the
273 field, scaled linearly to the literature spectra of Vandaele et al. (1998) at 296 K and Volkamer
274 et al. (2005) at 294 K, respectively. The literature spectra from Stutz et al. (2000), Meller et
275 al. (1991), Harder & Brault, (1997), and Keller-Rudek et al. (2013) are used for HONO,
276 methylglyoxal, H₂O, and O₄, respectively. The fitting range was 438 – 467 nm for the 455
277 nm channel, and 362 – 387 nm for the 365 nm channel. No structure was observed in the fit
278 residuals. Because the 455 nm channel has higher precision, only those NO₂ data are
279 presented here, although the two channels agree to within 3%. The data are averaged to 1 s.
280 The reported uncertainties are ± (9% + 0.6 ppbv) for HONO and ± (5% + 0.26 ppbv) for
281 NO₂.

282

283 2.2.5 Iodide-Adduct Chemical Ionization Mass Spectrometry (HONO)

284

285 HONO was measured using a modified commercial time of flight chemical ionization mass
286 spectrometer (TOF CIMS, Aerodyne Research, Inc.; Lee et al., 2014; Veres et al., 2020).
287 Trace gases are ionized by mixing ambient air with reagent ions made in flight, and the
288 resulting product ions are detected. Ions are separated by mass-to-charge ratio (m/z) using a
289 time-of-flight mass spectrometer with a resolving power of 5000 m/Δm and a range of mass
290 to charge ratio up to 494 m/z. Spectra were obtained at a 25 kHz repetition rate, and then
291 averaged to 1 s. High resolution peak fitting was performed on the spectra, using over 500
292 known masses. Reagent ions were formed by flowing 1 slpm N₂ through a temperature
293 controlled CH₃I permeation tube followed by a 20 mCi ²¹⁰Po radioactive source. Two reagent



294 ions are generated: Iodide ions (I^-) are formed in the radioactive source, and iodide-water
295 clusters ($I^- \cdot H_2O$) are formed when I^- reacts with water in the ion-molecule reactor (IMR). In
296 the IMR, the reagent ions cluster with analyte gases to form a stable iodide adduct. The IMR
297 was controlled at 40 mbar pressure to reduce the effects of secondary ion chemistry that
298 increase at higher pressures.

299

300 Ambient air was sampled through a mass flow controlled (6 slpm) heated perfluoroalkoxy
301 (PFA) inlet (70 cm length, 0.64 cm inner diameter). A pressure control region upstream of a
302 critical orifice at the entrance to the IMR was maintained at 140 mbar, so that a constant flow
303 of 1.2 slpm ambient air entered the IMR to mix with the 1 slpm ion source flow. A small
304 nitrogen flow of about 20 sccm containing water vapor was added directly into the IMR
305 region and controlled to maintain a measured $I^- \cdot H_2O : I^-$ cluster ratio of $50 \pm 2\%$, in order to
306 maintain constant detection sensitivity. The reagent ion signals during FIREX-AQ were
307 typically 2 MHz for $I^- \cdot H_2O$ and 4 MHz for I^- , and they were stable as a function of aircraft
308 altitude. In the most concentrated fire plumes with CO over 7 ppm, the abundance of
309 reactants reduced the reagent ion signals by up to 15%. The product cluster ions were
310 normalized by the iodide signals to account for changes in reagent ions. The instrument
311 background signal was determined inflight by overflowing the inlet with scrubbed ambient
312 air for 30 seconds every 10 minutes through a port located 2 cm downstream of the inlet
313 entrance. Calibrations with Cl_2 and HNO_3 permeation sources were performed hourly in
314 flight to diagnose the stability of instrument sensitivity.

315

316 HONO was detected as a cluster with I^- that has a mass to charge ratio of 173.90575 m/z.
317 Contributions from the ^{13}C isotope of formic acid at 173.91342 m/z are not completely mass
318 resolved but are accounted for using high resolution peak fitting and isotope ratios based on
319 the formic acid signal at its most abundant isotope. We know of no other contributions to the
320 signal at the mass used for HONO detection, consistent with previous studies (Neuman et al.,
321 2016). The background HONO signals were typically equivalent to a mixing ratio of 40 ppt,
322 and these were subtracted from the total signal to determine ambient HONO. Sensitivity to
323 HONO was determined in the laboratory, using a tunable, calibrated HONO source that uses
324 HCl reactions on humid $NaNO_2$ to generate HONO (Lao et al., 2020). The output was
325 calibrated spectroscopically using the NOAA ACES instrument (Min et al., 2016). The
326 absolute sensitivity to HONO was 3.4 ion counts/s/pptv for typical conditions. Sensitivities
327 normalized by the reagent ions are used to determine mixing ratios from the normalized
328 product ion signals. The HONO measurement uncertainty at fixed temperature was $\pm (15\% +$
329 $3 \text{ pptv})$, where the first term was from the laboratory calibrations and the second was the
330 variability of the in-flight background determinations. The HONO measurement precision
331 was $\pm 2 \text{ pptv}$ for 1 second data. Calibrations and field work conducted subsequent to FIREX-
332 AQ identified a temperature dependence to the CIMS calibration. Section 3.3 below
333 describes this sensitivity in more detail.

334

335 2.2.6 ΣNO_y



336 To determine the extent of budget closure for reactive odd nitrogen species during FIREX-
337 AQ, we compare measured NO_y (see section 2.2.1) with ΣNO_y defined as:

338

$$339 \quad \Sigma\text{NO}_y = \text{NO}_x + \text{HONO} + \text{HNO}_3 + \text{pNO}_3 + \text{APNs} \quad (\text{Eq. 2})$$

340

341 Other nitrogen oxides were also measured during FIREX-AQ but were not included in this
342 equation as they contributed on average less than 7% to the NO_y budget (see section 3.4).
343 Further, including these measurements would have decreased data availability for comparison
344 with the total NO_y measurement by more than 60%. These minor NO_y species are alkene
345 hydroxy nitrates, nitromethane (CH_3NO_2), N_2O_5 , and $\text{C}_1\text{--C}_5$ alkyl nitrates. ClNO_2 was also
346 measured by I-CIMS but not included in this work as its contribution to the NO_y budget was
347 negligible during FIREX-AQ.

348

349 • HNO_3 observations were made by the California Institute of Technology Chemical
350 Ionization Mass Spectrometer (CIT-CIMS) compact time-of-flight (cToF,
351 ToFwerk/Caltech) sensor using CF_3O^- ion chemistry (Crounse et al., 2006). In short,
352 a large flow of ambient air was rapidly brought into the aircraft through a Teflon
353 coated glass inlet (warmed slightly above ambient temperature), where it was
354 subsampled, diluted with dry N_2 , reacted with CF_3O^- , and underwent subsequent
355 product ion analysis by time-of-flight mass spectrometry. The $\text{HF}\cdot\text{NO}_3^-$ (m/z 82)
356 product ion is used to quantify HNO_3 . The hydroxy nitrates produced from the
357 oxidation of isoprene, ethene, propene, and butene are detected as cluster ions. In-
358 flight instrumental zeros were performed every ~15 minutes using dry N_2 and ambient
359 air passed through NaHCO_3 -coated nylon wool. Laboratory-generated, water-
360 dependent calibration curves were performed to produce ambient mixing ratios from
361 raw signals. Continuous HNO_3 data, with the exception of zero and calibration
362 periods, are reported with 1Hz frequency with an uncertainty of \pm (30%+ 50 pptv).

363

364 • Particulate nitrate (pNO_3) was measured with a high-resolution time-of-flight AMS
365 (HR-AMS, Aerodyne Research, Inc., Billerica, MA, USA). The HR-AMS measured
366 submicron ($\text{PM}_{0.9}$; calibrated in the field as described in Guo et al., 2021) aerosol
367 composition at high time resolution (0.1–1 s) by flash vaporization of the aerosol, 70
368 eV electron ionization of the volatilized gas phase and subsequent analysis by mass
369 spectrometry (Canagaratna et al., 2007; DeCarlo et al., 2006). pNO_3 is detected in the
370 HR-AMS as the sum of H_xNO_y^+ ions (mostly NO^+ and NO_2^+). Typical 1 s detection
371 limits for pNO_3 were about 90 ng sm^{-3} (30 pptv) for urban/background conditions.
372 Given the size cut in the HR-AMS instrument, pNO_3 does not include coarse nitrate
373 from the reaction of HNO_3 with sea salt or dust aerosol. It does include particulate
374 organic nitrates (pRONO_2 ; Day et al., 2021; Farmer et al., 2010), which are speciated
375 using the algorithm described in Fry et al. (2013) and Day et al. (2021). Likewise,
376 particulate aryl nitrates such as nitrocatechol also contribute to the total pNO_3 signal
377 (Guo et al., 2020). Nitrocatechol was also characterized by extractive electrospray
378 ionization time-of-flight mass spectrometry (EESI-MS; Pagonis et al., 2021) and



- 379 positive matrix factorization and tracer analysis suggests that total aryl nitrates could
380 be 3–7 times the concentration of nitrocatechol.
381
- 382 • APNs were measured using a thermal dissociation – chemical ionization mass
383 spectrometer (TD-CIMS) method. The CIMS instrument used during the FIREX-AQ
384 campaign was similar to that described in Slusher et al. (2004) and Lee et al. (2020).
385 Briefly, ambient air is sampled into the TD-CIMS through heated Teflon tubing at a
386 temperature of approximately 150°C to thermally dissociate APNs. The thermal
387 dissociation region was maintained at a constant pressure of 60 torr using a
388 commercial pressure controller (MKS 640) to minimize negative interference due to
389 NO, NO₂ and radical-radical reactions. In-flight calibrations were performed by
390 continuous addition of isotopically labeled peroxyacetyl nitrate (PAN) standard
391 quantified as acetate ion (61 m/z; C¹³H₃C¹³(O)O⁻) in the TD-CIMS. NO was
392 periodically added to the inlet (~10 ppm) to react away peroxyacetyl radicals and thus
393 to measure the instrument background signal.
394
 - 395 • Nitromethane (CH₃NO₂), along with other volatile organic compounds (VOCs), was
396 measured by proton-transfer-reaction time-of-flight mass spectrometry (PTR-ToF-
397 MS; Gkatzelis et al., in prep). The PTR-ToF-MS sampled VOCs at 5Hz through short
398 (1 m) heated inlet. Periodically, instrument backgrounds were determined by passing
399 ambient air through a platinum catalyst heated to 350°C. The instrument response to
400 VOCs was calibrated by gravimetrically prepared standards or by liquid calibration,
401 as described by Gkatzelis et al. (2021). CH₃NO mixing ratios were determined by
402 liquid calibration with an uncertainty of 30%.
403
 - 404 • N₂O₅ was detected as a cluster with I⁻ at mass 234.88574 m/z. Sensitivity was
405 determined by standard addition laboratory calibrations, with N₂O₅ generated by
406 reacting a NO₂ calibration standard with O₃ (Bertram et al., 2009), and quantified
407 using cavity ring down NO_y measurements (Womack et al., 2017). For typical
408 operating conditions during FIREX-AQ, N₂O₅ sensitivity was 70 ion counts/s/ppt.
409 N₂O₅ was measured with ± (15% + 2 pptv) accuracy and 0.1 pptv precision for 1
410 second data. Iodide ions cluster with a DMS oxidation product, hydroperoxymethyl
411 thioformate (HPMTF), that has a mass only 0.0074 amu greater than N₂O₅, and these
412 two molecules cannot be completely resolved spectrometrically with the resolution
413 (m/Δm = 5000) of this instrument (Veres et al., 2020). For these measurements over
414 the continent, the contribution from HPMTF to the signal at the iodide N₂O₅ cluster is
415 assumed to be negligible.
416
 - 417 • C₁–C₅ alkyl nitrates were measured by the NOAA integrated whole air sampling
418 system with off-line analysis by gas chromatography-mass spectrometry (iWAS/GC-
419 MS as described in Lerner et al. (2017)). There were 142 iWAS samples collected
420 over the LA Basin with an average fill time of 5.2 ± 0.7 seconds. There were 897
421 wildfire samples and 467 eastern fire samples with average fill times of 7.6 ± 1.1 and



422 4.5 ± 0.8 seconds, respectively. Due to the relatively fast fill times and targeted, on-
423 demand sampling capabilities of the iWAS, 88% and 74% were “full smoke” samples
424 for wildfire and eastern fire samples, respectively. All samples were analyzed in the
425 NOAA Chemical Science Laboratory within 213 hours of sample collection with an
426 average sample age of 87 ± 34 hours between sample collection and sample analysis
427 for FIREX-AQ.

428

429 2.2.7 Integrated Cavity Output Spectroscopy (CO)

430 CO was measured using a modified commercial off-axis ICOS instrument (Los Gatos
431 Research (LGR) N₂O/CO-30-EP; Baer et al., 2002) at approximately 4.6 μm . The
432 commercial instrument has two flow paths, a slow flow path with cavity pressure controlled
433 by an internal proportional valve, and a parallel high flow path with a needle valve to control
434 pressure. The instrument was modified to use only the high flow path, but with an automatic
435 cavity pressure controller. The needle valve was removed from the flow path in favor of a
436 Piezo proportional valve (Horiba Stec UR-Z732M) located near the inlet.

437

438 Air was sampled from a ram-air intake inlet through 0.64 cm (outside diameter) stainless
439 steel tubing. Cavity pressure was maintained at 85.0 ± 0.2 Torr in flight. Immediately inside
440 the fuselage, two CO (and N₂O) calibration gas standards known to within ± 0.4 ppb CO were
441 regularly delivered to the inlet line during flight to evaluate instrument sensitivity between
442 58.4 and 993.3 ppb CO (all ICOS-CO mixing ratios are reported as dry air mole fractions).
443 The calibration standards were added to displace ambient air and overflow the inlet, and were
444 calibrated before and after the project using standard tanks tied to the World Meteorological
445 Organization CO_X2014A scale from the NOAA Global Monitoring Laboratory (Hall et al.,
446 2007; Novelli et al., 1991). The 1-sigma variability of the slope and intercept of all in-flight
447 calibrations was 0.6% and 0.9 ppb, respectively. A third calibration standard, referred to as a
448 “target” (Peischl et al., 2010), was regularly introduced to the inlet between calibrations and
449 treated as an unknown to evaluate long-term instrument performance. The retrieved value of
450 109 in-flight targets during FIREX-AQ was 301.6 ± 1.0 ppb CO compared with the
451 calibrated value of 301.1 ± 0.4 ppb. The precision of the measurement in flight is estimated to
452 be 0.4 ppb.

453

454 After the campaign, the H₂O measurement was calibrated using a MBW 373LX chilled-
455 mirror hygrometer (MBW Calibration AG; Rollins et al., 2020). The H₂O measurement is
456 estimated to have an uncertainty of $\pm (50 \text{ ppmv} + 4\%)$, and was used to convert the CO
457 measurement to a dry air mole fraction. The uncertainty of the dry air mole fraction of CO is
458 estimated to be $\pm (2.0 \text{ ppb} + 2\%)$ for mixing ratios below 1 ppm.

459

460 2.2.8 Tunable Diode Laser Absorption Spectroscopy (CO)

461 Carbon Monoxide (CO) was measured by tunable diode laser absorption spectroscopy
462 (TDLAS) using the DACOM (Differential Absorption Carbon monOxide Measurement)
463 instrument (Sachse et al., 1987). The TDLAS instrument configuration used during FIREX-
464 AQ also included channels for measurements of methane (CH₄) and carbon dioxide isotopes
465 (¹²CO₂ and ¹³CO₂). This instrument utilizes three single-mode tunable diode lasers, with CO



466 measured using a quantum cascade laser (QCL) at approximately 4.7 μm . The three
467 individual mid-infrared laser beams were combined by the use of dichroic filters and directed
468 through a small volume (0.3 liter) Herriott cell enclosing a 36-meter optical path. After
469 exiting the Herriott cell, the beams were spectrally separated and directed to individual
470 HgCdTe (MCT) detectors.

471
472 The lasers were operated in a wavelength-modulated mode, each at an independent
473 frequency, and line-locked to the centers of the species' selected absorption lines. Lines were
474 selected to provide both good sensitivity and good isolation from any potential spectral
475 interferences. Detector signals were demodulated at twice the lasers' modulation frequencies
476 (2F detection), and normalized by average detected laser intensity.

477
478 Ambient air was sampled through an inlet probe, compressed, and passed through a
479 permeable membrane dryer to remove water vapor prior to being introduced into the Herriott
480 cell. Due to the need for very fast time response during FIREX-AQ, the instrument was
481 operated with a flow of approximately 14 slpm with the Herriott cell at a pressure of
482 approximately 67 mbar. The resulting time response, verified with a fast-acting valve, was
483 faster than 0.2 s. Data were reported at both 0.2 s and 1 s timesteps.

484
485 The TDLAS instrument was calibrated using the same gas standards as for the ICOS
486 instrument, nominally with a 4-minute period, but often advanced or delayed in time to avoid
487 calibrating during fire plume encounters. Calibrations provided both slope and intercept
488 values tying signals to species concentrations. The very large CO concentrations encountered
489 necessitated post-campaign correction calibrations to account for response nonlinearity.

490
491 Post-campaign analysis of the TDLAS CO data indicated that measurement precision (1σ)
492 was approximately 0.1% at 1 s and 0.14% at 0.2 s. Accuracy was dependent on CO mixing
493 ratio, and varied from 2% to 7%.

494

495 2.2.9 H₂O

496 H₂O was measured using the NASA diode laser hygrometer, an open-path infrared absorption
497 spectrometer that uses a laser locked to one of three water vapor absorption features near
498 1.395 μm , depending on the abundance of water vapor (Diskin et al., 2002; Podolske et al.,
499 2003). H₂O mixing ratios were determined with an uncertainty of 5%.

500

501 2.2.10 Smoke age

502 The age of smoke from emission to sampling by the aircraft was determined from an
503 ensemble of upwind trajectories from the aircraft (Holmes et al., 2020). Trajectories were
504 computed with HYSPLIT (Stein et al., 2015) using three meteorological datasets (HRRR,
505 NAM CONUS Nest, and GFS 0.25°). In each of the three trajectories, the advection time was
506 determined from the point where the trajectory most closely approached the source fire. The
507 age also includes plume rise time from the surface to trajectory altitude, which was estimated
508 with a mean rise time of $7 \pm 4 \text{ m s}^{-1}$ (Lareau et al., 2018). Trajectories and ages that were
509 grossly inconsistent with smoke transport patterns seen in geostationary satellite images were



510 excluded from further analysis. The ensemble of age estimates was then averaged to provide
511 a best estimate of smoke age. The median uncertainty in smoke age is about 27%, as
512 determined by spread among the ensemble of estimates.

513

514 2.3 Methodology

515 This study focuses on comparing the different techniques used for the measurements of one
516 or several reactive nitrogen species as well as CO during FIREX-AQ. Here we compare both
517 archived 1 s data (<https://www-air.larc.nasa.gov/missions/firex-aq/index.html>) and the plume-
518 integrated data. Plume-integrated data are obtained from integrating the 1Hz data of a given
519 measurement over a smoke plume transect. A smoke plume transect was identified using the
520 time period between a CO and/or black carbon (BC) increase above a local background value
521 (beginning of the plume transect) and the CO and/or BC decrease back to a background value
522 (end of the plume transect). Background values on either side of a plume were different for
523 some fires in spatially heterogeneous source regions. Note that any 10 s period of background
524 air, even if experienced during a single smoke plume transect, was sufficient to mark the end
525 of one transect and the start of the next. All 1Hz data were time-aligned prior to comparison
526 by synchronizing features in the time series of each species. Time shifts were typically less
527 than 4 seconds. Some disagreement between measurement techniques is expected due to the
528 rapid variations sampled during FIREX-AQ, particularly when those variations occur faster
529 than the measurement period and/or with greater spatial heterogeneity than the distance
530 between the sampling locations on a large aircraft that can reach 25m in some cases.

531

532 We first calculated the slope of the linear least-squares (LLS) orthogonal distance regression
533 (ODR) to characterize the percent difference between measurements of a pair of instruments
534 weighted by the inverse of the instrument precision. Here, we used a mixing ratio-
535 independent instrument precision that corresponded to the 1σ precision in clean air.

536 Weighting the fit by this term, rather than a more accurate but labor-intensive mixing-ratio-
537 dependent precision, tend to overweight the highest measured mixing ratios. The slope and
538 intercept resulting from the ODR regression analysis provide a measure of systematic or
539 species-dependent instrumental biases. Additionally, we calculated the difference between a
540 given pair of measurements. The difference, noted ΔY_{X1-X2} where X1 and X2 are the two
541 measurement techniques for detection of the Y species, provides an understanding of the
542 temporal evolution and environmental dependency of instrumental discrepancies. Note that
543 the regression analysis yields slightly different information than the calculation of the
544 difference: while the former is weighted more by fire plumes, where mixing ratios were
545 greatest, the latter is weighted more by background conditions, where most of the
546 measurements took place. Unless specified otherwise, all data available (i.e., both
547 background and fire smoke data) were included in the following comparisons. We also
548 calculated the fractional error ($FE = \Delta Y_{X1-X2}/Y_{avg}$ where $Y_{avg} = (Y_{X1} + Y_{X2})/2$) between pair
549 of instruments using specifically fire smoke data to minimize measurements below
550 instrument detection limits (Figures S1 and S2).

551

552 3 **Flight data comparisons**

553 3.1 NO



554 3.1.1 Campaign-wide comparison

555 The 1Hz data comparison between the CL and LIF instruments is shown in Figure 2. The
556 overall comparison slope (\pm combined instrument uncertainties) is 0.98 ± 0.08 ($R^2 = 0.93$)
557 with an intercept of -2 ± 0 pptv (Figure 2a). Figures 3a and 4a show the two instruments'
558 response in smoke from a wildfire and an eastern fire, respectively. While the NO signals
559 track each other remarkably well, there is a difference in time response that is typical of the
560 entire campaign. Figure S3 shows an expanded view of 10Hz NO and CO measurements in a
561 partial smoke plume transect, including the transition from smoke to background air
562 sampling. The NO signal in the CL instrument exhibits less structure than in the LIF
563 instrument and a tail following the plume-to-ambient air transition. These tails were
564 commonly observed during this transition. This effect in the CL instrument may partly
565 explain the elevated scatter below the 1:1 line in Figure 2b. Integrating the NO signal across
566 plume passes reduces the scatter due to different instrument time response: the regression
567 analysis of smoke plume-integrated NO mixing ratios yields a slope of 0.99 ($R^2 = 0.95$) for
568 the whole dataset (Figure 2c).

569
570 A histogram of the absolute difference between LIF and CL ($\Delta\text{NO}_{\text{LIF-CL}}$) is shown in Figure
571 5a. 90% of the values were between -44 and 43 pptv, and the whole dataset is normally
572 distributed around 0 ± 0 pptv (central value of the Gaussian fit and standard deviation).
573 $\Delta\text{NO}_{\text{LIF-CL}}$ exhibits no significant correlation with NO and H₂O mixing ratios, which suggests
574 that there was no systematic bias between the two instruments over a wide range of NO
575 mixing ratios and environmental conditions (Figures S4a and 6a). Similar slopes and
576 intercepts were obtained when separately comparing NO measurements during the wildfire,
577 eastern fire, and LA Basin sampling periods (Figures 2b and S5).

578

579 3.1.2 Literature aircraft NO measurement comparisons

580 Overall, the comparison between the two NO instruments shows an agreement within stated
581 uncertainties. While the single-photon LIF detection of NO is a new technique that was
582 evaluated for the first time during FIREX-AQ (Rollins et al., 2020), there are several studies
583 that compared CL detection of NO to other measurement techniques during airborne field
584 campaigns. The Global Tropospheric Experiment Chemical Instrumentation Test and
585 Evaluation (GTE-CITE) was designed in the 1990's to intercompare airborne measurement
586 techniques for trace species including NO, NO₂ and CO. Comparison of two CL instruments
587 and a two-photon LIF instrument showed agreement when NO mixing ratios were higher
588 than 50 pptv, but pointed out periods of disagreement when NO mixing ratios were lower
589 than 20 pptv (Gregory et al., 1990; Hoell et al., 1987). The Deep Convective Clouds &
590 Chemistry (DC3) experiment in 2012 allowed for side-by-side comparison of instruments
591 aboard two aircrafts at two level flight legs (7 and 12 km) for flight periods spanning 20–30
592 minutes. Pollack et al. (2016) showed that these NO measurements from two CL instruments
593 agreed within 2% for NO mixing ratios up to 1 ppbv. More recently, Sparks et al. (2019)
594 reported an intercomparison of several NO_y species measurements, including NO, from the
595 Wintertime Investigation of Transport, Emissions, and Reactivity (WINTER) airborne
596 experiment over the Northeast US in 2015. During WINTER, NO measured by CRDS and
597 CL differed on average by 16 % across all flights, which is outside of the combined



598 instrument uncertainties. CL measurements were more consistent with an independent
599 calculation of NO based on a photostationary state assumption.

600

601 3.2 NO₂

602 3.2.1 Campaign-wide comparison

603 Three instruments measured NO₂ mixing ratios during FIREX-AQ using CL, CES and LIF
604 detection techniques. The 1Hz data comparison between all three instruments is shown in
605 [Figure 7](#). We find that the LIF and CES overall comparison yields a slope (\pm combined
606 instrument uncertainties) of 1.03 ± 0.08 ($R^2 = 0.98$), well within the combined instrument
607 uncertainties of 8% ([Figure 7c](#)). However, we find that comparing either the LIF or CES
608 instruments to the CL instrument results in correlation slopes (\pm combined instrument
609 uncertainties) ranging from 0.88 ± 0.12 to 0.90 ± 0.11 ($R^2 = 0.97$), comparable to the 8–11%
610 combined uncertainties for each pair of instruments ([Figures 7a and b](#)). The higher NO₂
611 mixing ratios measured by the CL instrument are further illustrated in the time series in
612 [Figures 3b and 4b](#), and is consistent with a calibration error in one or all instruments, or an
613 interference from another species in the CL instrument. HONO is a known source of
614 interference in measured NO₂ by instruments that use photolysis in the near-UV region
615 (Pollack et al., 2011). However, this interference was determined to be low (less than 5% of
616 HONO concentration) following laboratory tests using a HONO calibration source (Lao et
617 al., 2020), and the NO₂ measurement by CL was corrected for it. Additionally, we did not
618 find a correlation between either $\Delta\text{NO}_{2\text{CES-CL}}$ or $\Delta\text{NO}_{2\text{LIF-CL}}$ and HONO mixing ratios. There
619 was better agreement between the CL and the other two instruments when sampling the
620 wildfires (slopes of 0.91) than the eastern fires (slopes of 0.75 and 0.87 for the LIF and CES,
621 respectively) ([Figures 7d and e](#)). Similarly, the agreement between the CES and the LIF
622 instruments was near perfect during the first period (slope of 1.00), but worse during the
623 latter period (slope of 1.13; [Figure 7f](#)). Note that the LIF instrument did not report data for
624 three flights out of seven during the eastern fires sampling period. The increased difference
625 may be caused by the physical distance between instrument inlets combined with higher
626 spatial heterogeneity of trace gases in the smaller and thinner eastern fire plumes, although
627 higher mixing ratios of a potential interferent may still exist. Non-acyl peroxy species
628 such as pernitric acid (HO₂NO₂) and methyl peroxy nitrate (MPN) can be abundant in smoke
629 plumes and interfere with NO₂ measurements (Browne et al., 2011; Nault et al., 2015). This
630 interference is the result of the thermal dissociation of HO₂NO₂ and MPN in heated inlets and
631 sampling lines, and impact differently each instrument depending on their flush time. During
632 FIREX-AQ, the CES and CL instruments had similar flush time of about 750ms meaning that
633 the thermal decomposition of non-acyl peroxy species is unlikely to explain the 10–12%
634 higher NO₂ signal in the CL instrument. Nitrated phenolic compounds can be abundant in
635 aged smoke (Decker et al., 2021), and have large UV cross sections (Chen et al., 2011). They
636 are unlikely to contribute to the interference as their NO₂ photolysis quantum yields are very
637 low. Nevertheless, further laboratory work on the NO₂ interference of such species in
638 photolytic converters is of interest. The agreement between all three instruments for
639 individual flights was generally within combined instrument uncertainties, but with some
640 variability ([Figures S6–S8](#)).

641



642 Histograms of the absolute difference between CES, LIF and CL ($\Delta\text{NO}_{2\text{LIF-CL}}$, $\Delta\text{NO}_{2\text{CES-CL}}$
643 and $\Delta\text{NO}_{2\text{CES-LIF}}$) are shown in Figures 5b–d. 90% of $\Delta\text{NO}_{2\text{LIF-CL}}$, $\Delta\text{NO}_{2\text{CES-CL}}$ and $\Delta\text{NO}_{2\text{CES-}}$
644 LIF values were between -298 and 338 pptv, -469 and 302 , and -576 and 393 pptv,
645 respectively, and all are normally distributed around the central value of the Gaussian fit of
646 0.038 ± 0.001 , -0.052 ± 0.001 , and -0.071 ± 0.001 , respectively. $\Delta\text{NO}_{2\text{LIF-CL}}$, $\Delta\text{NO}_{2\text{CES-CL}}$
647 and $\Delta\text{NO}_{2\text{CES-LIF}}$ exhibit no significant trend with H_2O mixing ratios (Figures 6b–d), yet
648 $\Delta\text{NO}_{2\text{LIF-CL}}$ and $\Delta\text{NO}_{2\text{CES-CL}}$ were weakly ($R^2 = 0.36$ and 0.31 , respectively) correlated with
649 the absolute NO_2 mixing ratio (Figures S4b and d).

650

651 3.2.2 Literature aircraft NO_2 measurement comparisons

652 Previous comparisons of NO_2 airborne measurements often show periods of disagreement
653 between instruments, although there were some occasions where instruments agreed within
654 stated uncertainties. During the GTE-CITE experiment, the comparison of NO_2
655 measurements using a two-photon NO LIF system with laser photolysis of NO_2 to NO with a
656 CL detector equipped with a xenon arc lamp for NO_2 photolysis into NO showed agreement
657 within 30–40% (Gregory et al., 1990). Pollack et al. (2016) showed that two NO_2
658 measurements, both using CL but each in a different aircraft, agreed within 28% during the
659 DC3 campaign. During WINTER, NO_2 measurements by CRDS and LIF agreed with an
660 average proportional bias of 2% across all flights – well within combined uncertainties
661 (Sparks et al., 2019). During SENEX, three techniques were used to measure NO_2 : a CRDS
662 instrument, a CES instrument and a CL instrument. The agreement between CRDS and CES
663 measurements with the CL technique was on average 6 and 10% (Warneke et al., 2016).

664

665 3.3 HONO

666 3.3.1 Campaign-wide comparison

667 The 1Hz data comparison between the CES and the CIMS instruments is shown in Figure 8,
668 and timeseries of HONO measurements in wildfires and eastern fires are shown in Figures 3c
669 and 4c, respectively. The correlation between the CES and CIMS was very high in each
670 plume transect (Figures 3c and 4c), but the overall comparison yielded a slope (\pm combined
671 instrument uncertainties) of 1.80 ± 0.16 ($R^2 = 0.77$) and an intercept of -0.12 ± 1.10 ppbv
672 (Figure 8a). Integrating across plume transects yielded a slope of 1.34 ± 0.16 (Figure 8c). The
673 CIMS consistently reported less HONO than the CES in smoke plumes, and the average
674 slope between the two measurements was considerably greater during the eastern fires
675 compared to the wildfires (Figures 8b and S9). However, flight averages of the absolute
676 difference between the two measurements ($\Delta\text{HONO}_{\text{CES-CIMS}}$) ranged between -332 and 245
677 pptv throughout the campaign and were similarly scattered around zero during the two
678 different time periods (Figure S9). A histogram of $\Delta\text{HONO}_{\text{CES-CIMS}}$ is shown in Figure 5e.
679 90% of the values were between -965 and 880 pptv, and the whole dataset is normally
680 distributed around the central value of the Gaussian fit (\pm standard deviation) of -119 ± 2
681 pptv. $\Delta\text{HONO}_{\text{CES-CIMS}}$ exhibits no significant slope with HONO (Figure S4e). While the
682 deployment out of Salina was operated under noticeably more humid conditions (H_2O ranged
683 from 0.002 to 2.944%) than out of Boise (H_2O ranged from 0.004 to 1.479%), we find no
684 significant correlation between $\Delta\text{HONO}_{\text{CES-CIMS}}$ and H_2O mixing ratios (Figure 6e).

685



686 However, further laboratory studies, field measurements, and examination of this comparison
687 has revealed that the CIMS sensitivity to HONO is reduced when the instrument reaches
688 temperatures greater than 30°C (Figure S10). This sensitivity dependence on temperature
689 does not affect all compounds measured by the CIMS, and the sensitivity to Cl₂ and HNO₃
690 used for in-flight calibrations was independent of instrument temperature. The aircraft cabin
691 temperature was greatest during the eastern agricultural flights, when the CIMS instrument
692 temperatures were often 40°C and far greater than the typical 25°C instrument temperatures
693 in the laboratory when the CIMS HONO sensitivity was determined. As a consequence, the
694 reported CIMS HONO values were spuriously low, especially during the eastern fires, and
695 particularly later in flights when the aircraft temperatures were greatest. This intercomparison
696 has yielded new insights into the CIMS HONO detection sensitivity, and future work will
697 identify and implement appropriate corrections to this measurement.

698
699 3.3.2 Literature aircraft and ground HONO measurement comparisons
700 HONO measurements are notoriously difficult due to the potential for artifacts associated
701 with inlet surfaces as well as interferences associated with some methods (e.g., Kleffmann et
702 al., 2006; Xu et al., 2019). Past ground-based intercomparisons often revealed significant
703 discrepancies in HONO measurements. For example, six ground-based HONO measurement
704 techniques including a CIMS instrument were compared during the Study of Houston
705 Atmospheric Radical Precursors (SHARP) campaign in 2009 (Pinto et al., 2014). While three
706 out of six of these techniques agreed within 20%, larger deviations were found when the
707 other three instruments were considered and attributed to the physical separation of these
708 instruments. Three different techniques, including a CIMS instrument, were used to measure
709 HONO in the urban area of Shanghai, China (Bernard et al., 2016). The percent difference
710 between these measurements ranged from 27 to 46%. In 2019, six HONO measurement
711 techniques were again compared in a Chinese urban area, this time in Beijing, and included a
712 CIMS instrument as well as two broadband cavity enhanced absorption spectrometers
713 (BBCEAS) (Crilley et al., 2019). Percent differences up to 39% were observed during this
714 intercomparison and again attributed to the physical distance separating inlets coupled to high
715 spatial heterogeneity of HONO mixing ratios. Airborne measurements of HONO by CIMS
716 and CES were made during the Southeast Nexus Experiment (SENEX), and the CES
717 instrument was approximately 25% higher than the CIMS instrument (Neuman et al.,
718 2016).

720 3.4 NO_y

721 3.4.1 Campaign-wide comparison

722 The 1Hz data comparison between the total NO_y measurement by CL and ΣNO_y is shown in
723 Figure 9. ΣNO_y definition is given by Eq. 2 (see section 2.2.8). C₁–C₅ alkyl nitrates and other
724 minor NO_y species (including N₂O₅, CH₃NO₂, and alkene hydroxy nitrates) contributed less
725 than 7% of the NO_y budget on average (Figure 10). The overall comparison yielded a slope
726 (± combined instrument uncertainties) of 1.00 ± 0.25 (R² = 0.98) and an intercept of -0.52 ±
727 0.01 ppbv (Figure 9a). The regression analysis of smoke plume-integrated NO_y mixing ratios
728 yields a slope of 1.00 (R² = 0.99) for the whole dataset (Figure 9c). Comparison of CL NO_y



729 to ΣNO_y in fresh (<1h since emission) and aged (>1h since emission) smoke during the
730 wildfires sampling period showed similar agreement (slopes of 0.98 and 1.05, respectively)
731 despite the chemical evolution of NO_y species, highlighted by the different proportion of
732 those species to the NO_y balance (Figure S11). Measurements used in Eq. 2 are CL NO_x ,
733 CIMS HONO, CIMS HNO_3 , HR-AMS pNO_3 and CIMS APNs. These measurements were
734 primarily used because they had better precision. Using LIF NO, CES NO_2 and CES HONO
735 as primary measurements changed the correlation slope between measured NO_y and ΣNO_y by
736 less than 5% (Figure S12).

737

738 Despite this correlation, two modes are apparent in the overall distribution of the absolute
739 difference ($\Delta\text{NO}_{y\text{CL-Sum}}$) between ΣNO_y and the total NO_y measurement (Figure 5f). The first
740 mode is distributed around -0.068 ± 0.001 ppbv (central value of the first mode of the
741 Gaussian fit), while the second is distributed around an average value of 0.158 ± 0.009 ppbv
742 (central value of the second mode of the Gaussian fit). Separating the comparison into three
743 time periods reveals that this two-mode distribution of $\Delta\text{NO}_{y\text{CL-Sum}}$ comes from the eastern
744 fires sampling period as well as from the LA Basin flights whereas during the wildfires
745 sampling period $\Delta\text{NO}_{y\text{CL-Sum}}$ distribution is unimodal (Figure 11).

746

747 Higher ΣNO_y compared to NO_y (first mode) could be explained by (i) a lower conversion
748 efficiency of one or more NO_y species in the CL instrument than estimated in the laboratory,
749 (ii) sampling loss of pNO_3 through the NO_y inlet, and (iii) inaccuracy in one of the individual
750 NO_y species measurement techniques. Here, we further investigated the sampling loss of
751 pNO_3 through the CL instrument NO_y inlet using a multistage flow model following the
752 template of the Particle Loss Calculator (von der Weiden et al., 2009). The model calculates
753 aerodynamic losses at each stage of the NO_y inlet and provides the resulting total pNO_3
754 sampling efficiency (See Section S1 and Figure SA). We find that the main aerosol sampling
755 loss occurs at the NO_y inlet tip orifice (1.0 mm in diameter) due to the inlet orientation
756 (perpendicular to the aircraft flight direction). Additional loss was calculated to be negligible
757 once pNO_3 penetrated the NO_y inlet, meaning that pNO_3 is fully volatilized into NO inside
758 the heated gold catalyst (See Section S1 and Figure SA). Particle sampling through the NO_y
759 inlet is highly dependent on altitude, air speed (see section S1 and Figure SB) and pNO_3 mass
760 size distribution (Figure 12a). Figure 12b shows the average modelled particle sampling
761 fraction through the NO_y inlet, given as a ratio where a value of 1 means the total pNO_3 is
762 sampled, for each flight during FIREX-AQ. Particle sampling fraction was calculated for
763 three different air speeds for each flight: 40%, 65%, and 100% of the aircraft speed. An
764 assumed sampled air speed of 65% that of the aircraft improved the correlation between
765 $\Delta\text{NO}_{y\text{CL-Sum}}$ and the modelled pNO_3 loss in the inlet (see Section S1 and Figure SB). At that
766 speed, the calculated average particle sampling fraction varied between 0.36 and 0.99 for
767 each flight (Figure 12b). Consequently, 0–24% of the measured NO_y in smoke (assuming a
768 sampled air speed 65% that of the aircraft) initially attributed to pNO_3 may result from other
769 reactive nitrogen species than those included in the ΣNO_y (Figure 12b). This additional
770 contribution has a large uncertainty because the model may underestimate pNO_3 sampling
771 through the NO_y inlet due to the large uncertainty when the losses are calculated at high air



772 speed (see Section S1). Further, we used bulk aerosol volume size distributions measured
773 with a Laser Aerosol Spectrometer (LAS; Moore et al., 2021) to derive $p\text{NO}_3$ sampling
774 fractions in Figure 12a as $p\text{NO}_3$ mass size distribution measurements were not available for
775 all flights during FIREX-AQ. At a typical FIREX-AQ sampling altitude of 5 km, the LAS
776 and HR-AMS size distributions can differ by about 10% (See Section S1 and Figure SC),
777 which adds to the uncertainty of the $p\text{NO}_3$ sampling fraction through the NO_y inlet.
778 Correcting for particle sampling through the NO_y inlet still yields an agreement between
779 measured NO_y and ΣNO_y that is within the combined instrument uncertainties of 25%.

780

781 On the other hand, the positive $\Delta\text{NO}_{y\text{CL-Sum}}$ mode (second mode) may indicate either an
782 inaccuracy in one of the individual NO_y species measurement techniques or an NO_y species
783 not measured. Further, we find that positive $\Delta\text{NO}_{y\text{CL-Sum}}$ occurred both in smoke (Figure 11d)
784 and in background air (Figure 11c) when sampling the eastern fires and that $\Delta\text{NO}_{y\text{CL-Sum}}$
785 exponentially decreased with altitude, a pattern also observed during the LA Basin flights but
786 not during the wildfires sampling period (Figure 13b). Note that flight altitude when
787 sampling the wildfires was 4.6 km on average, higher the altitude average of 0.6 and 1.1 km
788 during the eastern fires and the LA Basin flights, respectively. Both water vapor and $\text{C}_1\text{--}\text{C}_5$
789 alkyl nitrates (not included in ΣNO_y thus far) were enhanced at lower altitude and may be
790 possible causes for the positive $\Delta\text{NO}_{y\text{CL-Sum}}$ mode. Alkyl nitrates have been shown to account
791 for a significant fraction of the NO_y budget in past studies (e.g., Fisher et al., 2016; Hayden et
792 al., 2003; Horii et al., 2005). However, we find only a weak correlation between $\Delta\text{NO}_{y\text{CL-Sum}}$
793 and $\text{C}_1\text{--}\text{C}_5$ alkyl nitrates during both the wildfires ($R^2 = 0.07$) and eastern fires ($R^2 = 0.08$)
794 sampling periods (Figure 13c). The correlation is stronger ($R^2 = 0.44$) during the LA Basin
795 flights (Figure 13c). Further, we find that $\text{C}_1\text{--}\text{C}_5$ alkyl nitrates contributed similarly to the
796 NO_y budget when smoke from the wildfires (1.1% on average) and the eastern fires (0.8% on
797 average) was sampled (Figure 10a), while the positive mode in the $\Delta\text{NO}_{y\text{CL-Sum}}$ distribution is
798 present in the latter period only. H_2O is a known source of interference in most instruments,
799 and its impact on measurements is minimized when an accurate correction can be applied.
800 Increasing $\Delta\text{NO}_{y\text{CL-Sum}}$ is associated with increasing H_2O mixing ratios in the eastern fires,
801 although the correlation is weak ($R^2 = 0.05$) due to the elevated scatter of the data (Figure
802 13a). Similar slopes and intercepts were obtained when separately comparing NO_y
803 measurements in smoke from the wildfires and eastern fires (Figures 9b and S13). The slope
804 of 0.81 during the LA Basin flights, may be caused by the lower precision of ΣNO_y than that
805 of the CL NO_y (Figure 9b).

806

807 3.4.2 Discussion and other NO_y measurement comparisons

808 Overall, the agreement between the total NO_y measured by the CL instrument and the ΣNO_y
809 is within instrument uncertainties. Budget closure implies that the historical definition of NO_y
810 (*i.e.*, NO_x and its oxidation products, excluding reduced nitrogen species such as NH_3 and
811 HCN) is adequate even in extremely reactive conditions that foster rapid changes in NO_y
812 speciation. Reduced nitrogen species such as hydrogen cyanide (HCN) or ammonia (NH_3)
813 represent a large fraction of the total nitrogen emission from biomass burning (Roberts et al.,
814 2020) and have been shown to cause a small interference in CL instruments in dry air (Fahey



815 et al., 1985, 1986). This interference is often neglected because of either the low atmospheric
816 abundance of these species or sampling in humid air where such an interference is thought to
817 be negligible. Here, we find no evidence for a potential interference of HCN or NH₃, despite
818 their high abundance (tens of ppbv) in smoke plumes (Figure S14). Altogether, our findings
819 show that the NO_y instrument provides an accurate and conservative measurement of total
820 reactive nitrogen species, although further work is needed to empirically characterize pNO₃
821 sampling through the NO_y inlet.

822
823 There are a few studies that recently examined the NO_y budget closure from aircraft
824 measurements. Calahorrano et al. (2020) presented reactive odd nitrogen partitioning during
825 the Western wildfire Experiment for Cloud chemistry, Aerosol absorption and Nitrogen (WE-
826 CAN) that sampled western American wildfires during the summer 2018. The authors found
827 significant (15–26%) contribution of organic N species other than APNs and alkyl nitrates to
828 ΣNO_y. However, there was no total NO_y measurement during WE-CAN, and the conclusion
829 is based on summed individual reactive nitrogen species. The FIREX-AQ comparison of
830 ΣNO_y to total NO_y finds 2–13% of the total NO_y unaccounted for, smaller than the estimate of
831 a 15–26% contribution from multifunctional organic nitrates from WE-CAN. While the
832 FIREX-AQ NO_y difference suggests a smaller contribution from organic nitrates, the WE-
833 CAN estimate is within the uncertainty of the FIREX-AQ analysis. During the WINTER
834 campaign, budget closure of NO_z (=NO_y – NO_x) was demonstrated to occur within 20% for
835 all flights following the comparison of ΣNO_z with total NO_z from three different
836 measurement techniques, including a CL instrument (Sparks et al., 2019). A recent ground-
837 based study in New York State in the US found that the sum of the individual reactive odd
838 nitrogen species accounted for 95% of the total NO_y, well within measurement uncertainties
839 (Ninneman et al., 2021). These recent studies contrast with somewhat older literature that
840 often reported a significant shortfall in the NO_y balance, where measured NO_y was higher
841 than ΣNO_y (Hayden et al., 2003; Horii et al., 2005; Williams et al., 1997; Zhang et al., 2008).
842 This shortfall has often been attributed to unmeasured organic N species and more
843 specifically alkyl nitrates (Day et al., 2003; Horii et al., 2005). During FIREX-AQ, C₁–C₅
844 alkyl nitrates accounted for less than 7% on average of the NO_y budget (Figure 10),
845 consistent with findings from other regions in the US (Benedict et al., 2018; Russo et al.,
846 2010). However, FIREX-AQ did not include a measurement of total alkyl nitrates.

847

848 3.5 CO

849 3.5.1 Campaign-wide comparison

850 The 1Hz data comparison between the ICOS and the TDLAS instruments is shown in Figure
851 14. The overall comparison yielded a slope (\pm combined instrument uncertainties) of $0.98 \pm$
852 0.03 ($R^2 = 0.99$) and an intercept of -1.06 ± 0.01 ppbv (Figure 14a). The regression analysis
853 of smoke plume-integrated CO mixing ratios yields a slope of 0.99 ($R^2 = 1$) for the whole
854 dataset (Figure 14c). A histogram of the absolute difference between CO measurements
855 ($\Delta\text{CO}_{\text{ICOS-TDLAS}}$) is shown in Figure 5g. 90% of the values were between -6.05 and 2.35 ppbv,
856 and the whole dataset is normally distributed around the central value of the Gaussian fit of $-$
857 2.87 ± 0.02 ppbv. This is indicative of an offset between the two CO instruments, with the



858 TDLAS systematically higher than the ICOS instrument. This average 2.87 ppbv offset was
859 consistent throughout the campaign regardless of the type of fires that were sampled.
860 Therefore, it cannot explain the significantly lower agreement of the instruments during the
861 eastern fires compared to the wildfires sampling period (Figures 14b and S12). During the
862 first period, the overall slope was 0.99 and ranged from 0.97 to 1.02 (average of 0.99) for
863 individual flights, well within the combined instrument uncertainties of 3% (Figures 14b and
864 S12). However, all individual flight measurements during the eastern fires sampling period
865 exhibit slopes reduced by about 10% (range = 0.86–0.91 with an average of 0.89) and largely
866 positive intercepts (range 6.75–19.04 with an average of 11.51) (Figure S15). As observed for
867 other species, the second period proved to be a more challenging environment for CO
868 measurements. This may be attributed to a spectral issue with one or the other of these two
869 instruments, although we could not identify the source of the discrepancy. $\Delta\text{CO}_{\text{ICOS-TDLAS}}$
870 exhibit no significant slope with CO (Figure S4g) and H₂O (Figure 6g) mixing ratios.

871

872

3.5.2 Literature aircraft CO measurement comparisons

873 Overall, the comparison between the two CO instruments shows an agreement well within
874 stated uncertainties. We find that the agreement between the two CO instruments used during
875 FIREX-AQ is well in line with past intercomparisons. During the GTE-CITE experiment, the
876 comparison of a TDLAS technique with two grab sample/gas chromatograph methods for
877 detection of CO showed agreement across the instruments – within the combined instrument
878 uncertainties and strong correlations ($R^2 = 0.85\text{--}0.98$) for CO ranging from 60 to 140 ppbv
879 (Hoell et al., 1987). During the North Atlantic Regional Experiment (NARE 97) CO was
880 measured by TDLAS and vacuum ultra-violet fluorescence with agreement to within 11%
881 and systematic offsets of less than 1 ppbv (Holloway et al., 2000). CO was also more recently
882 measured by TDLAS and vacuum ultra-violet fluorescence during the side-by-side
883 comparison of instruments aboard two aircraft during the DC3 experiment. There, CO
884 measurements agreed within 5% during flight periods typically ranging from 20 to 30
885 minutes (Pollack et al., 2016).

886

887 4 Conclusion

888 In this study, we compare airborne measurements of NO, NO₂, HONO, NO_y and CO
889 conducted during the FIREX-AQ campaign in the summer 2019. This dataset offers the
890 opportunity to assess the accuracy of a large suite of detection techniques in a challenging
891 environment where species mixing ratios increased by tens of ppbv in seconds between
892 background air and fire smoke. For NO, NO₂ (CES and LIF), NO_y and CO, correlations agree
893 better than the combined instrument uncertainties, indicating that the stated individual
894 uncertainties are conservative estimates. For NO₂ (CL) and HONO, the percent difference
895 between measurements is higher than the combined instrument uncertainties, indicating
896 potential interferences or calibration inaccuracies that are not identified at this time. Based on
897 the analysis above, we make the following recommendations, which are specific to the
898 FIREX-AQ campaign.

899

900 1) Comparison of NO measurements by LIF and CL showed an overall agreement well
901 within instrument uncertainties. Flight-to-flight agreement was generally more variable



902 during the eastern fires sampling period than during the wildfires sampling period, which was
903 attributed to the heterogeneous nature of smoke plumes combined with the physical
904 separation of inlets. Both measurements are considered reliable for FIREX-AQ, although the
905 LIF instrument has better 1Hz precision (1 pptv) than the CL instrument (6 pptv), and the CL
906 instrument exhibited slower time response.

907

908 2) Comparison of NO₂ measurements by LIF and CES showed an overall agreement well
909 within the stated instrument uncertainties. However, NO₂ measured by CL is on average 10%
910 higher than that measured by the other two techniques. The agreement worsens for all
911 instruments when comparing NO₂ measured during the eastern fires sampling period, likely
912 for similar reasons as indicated for the NO measurements.

913

914 3) The CES and CIMS HONO measurements were highly correlated in each fire plume
915 transect, but the correlation slope of CES vs. CIMS for all 1 Hz data from the entire
916 campaign was 1.8. The HONO measured by CIMS was on average 74% of that measured by
917 CES during the wildfires sampling period, and on average 40% of CES during the eastern
918 fires sampling period. The higher precision data from the CIMS are most useful for analysis
919 of HONO when mixing ratios are lower. The redundancy of HONO measurements during
920 FIREX-AQ led to the discovery that the CIMS sensitivity to HONO was reduced in a high
921 temperature environment. This intercomparison has initiated further studies of the CIMS
922 sensitivity to HONO and other compounds.

923

924 4) Closure of the NO_y budget between the total NO_y measurement by CL and ΣNO_y was
925 achieved for all flights and correlation slopes were usually much better than the combined
926 instrument uncertainties of 25%. NO_x, HNO₃, HONO, APNs and pNO₃ are the main
927 contributors to the NO_y budget, with the other reactive N species contributing less than 10%
928 on average. We find that the modelled pNO₃ sampling fraction through the NO_y inlet is
929 highly dependent on altitude, air speed and pNO₃ mass size distribution, and varied on
930 average between 0.36 and 0.99 during FIREX-AQ. Therefore, approximately 0–24% on
931 average of the total measured NO_y by CL may be unaccounted for and possibly explained by
932 other species such as multifunctional organic nitrates. The reason for the secondary positive
933 mode of 0.4 ppbv in the ΔNO_{yCL-Sum} distribution in the eastern fires and LA Basin flights
934 could not be clearly identified. Potential explanations include the contribution of gas-phase
935 organic nitrates, not included in the ΣNO_y, and/or a water vapor interference in one or more
936 instruments. Regardless, we conclude that the total NO_y measurement by CL provides a
937 robust quantification of the reactive nitrogen species in background air as well as in smoke
938 plumes, and that the total NO_y measurement is not sensitive to interference from reduced
939 nitrogen species in fire plumes. Further laboratory and field work will be needed to fully
940 characterize pNO₃ sampling through the NO_y inlet.

941

942 5) Comparison of CO measurements by TDLAS and ICOS showed an agreement well within
943 the combined instrument uncertainties. An offset of ~2 ppbv between the two instruments
944 was identified but has little impact on the correlation. There was a clear difference in the



945 agreement between the wildfires sampling period and the eastern fires sampling period,
946 where the correlation slopes were about 10% lower.

947

948 6) Integrating data across smoke plume transects generally improved the correlation between
949 independent measurements and may be necessary for fire-science related analyses, especially
950 for smaller plumes with greater spatial heterogeneity compared to the distance between the
951 sampling locations on a large aircraft.

952

953 **Data availability**

954 All data used in this manuscript are archived online and available at [https://www-](https://www-air.larc.nasa.gov/cgi-bin/ArcView/firexaq)
955 [air.larc.nasa.gov/cgi-bin/ArcView/firexaq](https://www-air.larc.nasa.gov/cgi-bin/ArcView/firexaq).

956

957 **Author contribution**

958 I.B. and T.B.R. designed research. All authors performed FIREX-AQ measurements. P.C.-J.,
959 H. G., and J.L.J performed the flow modelling analysis. All authors analyzed data. I.B., J.P.,
960 J.A.N., and S.S.B. wrote the original draft and all authors edited and revised the paper.

961

962 **Competing interests**

963 The authors declare they have no conflict of interest.

964

965 **Acknowledgments**

966 We would like to thank the NOAA/NASA FIREX-AQ science and aircraft operation teams.
967 We acknowledge A. Whistaler, F. Piel and L. Tomsche for providing the NH₃ measurements
968 from FIREX-AQ. We thank A. Middlebrook for helpful discussion regarding pNO₃ sampling
969 in the NO_y inlet and AMS performance. IB, JP, JAN, SSB, MMC, JBG, GIG, AL, PSR,
970 MAR, AWR, RAW and CCW were supported by the NOAA Cooperative Agreement with
971 CIRES, NA17OAR4320101. VS acknowledges NOAA grant NA16OAR4310100. JMS and
972 TFH acknowledge support from the NASA Tropospheric Composition Program and NOAA
973 Climate Program Office's Atmospheric Chemistry, Carbon Cycle and Climate (AC4)
974 program (NA17OAR4310004). DP, BAN, HG, PCJ and JLJ were supported by NASA grant
975 80NSSC18K0630. LX, KTV, HA and POW acknowledge NASA grant 80NSSC18K0660.

976

977 **References**

- 978 Andreae, M. O. (2019). Emission of trace gases and aerosols from biomass burning – an
979 updated assessment. *Atmospheric Chemistry and Physics*, 19(13), 8523–8546.
980 <https://doi.org/10.5194/acp-19-8523-2019>
- 981 Baer, D. S., Paul, J. B., Gupta, M., & O'Keefe, A. (2002). Sensitive absorption measurements
982 in the near-infrared region using off-axis integrated-cavity-output spectroscopy.
983 *Applied Physics B*, 75(2), 261–265. <https://doi.org/10.1007/s00340-002-0971-z>
- 984 Balch, J. K., Bradley, B. A., Abatzoglou, J. T., Nagy, R. C., Fusco, E. J., & Mahood, A. L. (2017).
985 Human-started wildfires expand the fire niche across the United States. *Proceedings*
986 *of the National Academy of Sciences*, 114(11), 2946–2951.
987 <https://doi.org/10.1073/pnas.1617394114>
- 988 Benedict, K. B., Prenni, A. J., Sullivan, A. P., Evanoski-Cole, A. R., Fischer, E. V., Callahan, S., et
989 al. (2018). Impact of Front Range sources on reactive nitrogen concentrations and



- 990 deposition in Rocky Mountain National Park. *PeerJ*, 6, e4759.
991 <https://doi.org/10.7717/peerj.4759>
- 992 Bernard, F., Cazaunau, M., Grosselin, B., Zhou, B., Zheng, J., Liang, P., et al. (2016).
993 Measurements of nitrous acid (HONO) in urban area of Shanghai, China.
994 *Environmental Science and Pollution Research*, 23(6), 5818–5829.
995 <https://doi.org/10.1007/s11356-015-5797-4>
- 996 Bertram, T. H., Thornton, J. A., & Riedel, T. P. (2009). An experimental technique for the
997 direct measurement of N₂O₅ reactivity on ambient particles. *Atmospheric*
998 *Measurement Techniques*, 2(1), 231–242. <https://doi.org/10.5194/amt-2-231-2009>
- 999 Bollinger, M. J., Sievers, R. E., Fahey, D. W., & Fehsenfeld, F. C. (1983). Conversion of
1000 nitrogen dioxide, nitric acid, and n-propyl nitrate to nitric oxide by a gold-catalyzed
1001 reduction with carbon monoxide. *Analytical Chemistry*, 55(12), 1980–1986.
1002 <https://doi.org/10.1021/ac00262a034>
- 1003 Bowman, D. M. J. S., Balch, J. K., Artaxo, P., Bond, W. J., Carlson, J. M., Cochrane, M. A., et al.
1004 (2009). Fire in the Earth System. *Science*, 324(5926), 481–484.
1005 <https://doi.org/10.1126/science.1163886>
- 1006 Browne, E. C., Perring, A. E., Wooldridge, P. J., Apel, E., Hall, S. R., Huey, L. G., et al. (2011).
1007 Global and regional effects of the photochemistry of CH₃O₂NO₂: evidence from
1008 ARCTAS. *Atmospheric Chemistry and Physics*, 11(9), 4209–4219.
1009 <https://doi.org/10.5194/acp-11-4209-2011>
- 1010 Burke, M., Driscoll, A., Heft-Neal, S., Xue, J., Burney, J., & Wara, M. (2021). The changing risk
1011 and burden of wildfire in the United States. *Proceedings of the National Academy of*
1012 *Sciences*, 118(2). <https://doi.org/10.1073/pnas.2011048118>
- 1013 Calahorrano, J. F. J., Lindaas, J., O'Dell, K., Palm, B. B., Peng, Q., Flocke, F., et al. (2020).
1014 Daytime Oxidized Reactive Nitrogen Partitioning in Western U.S. Wildfire Smoke
1015 Plumes. *Journal of Geophysical Research: Atmospheres*, 126, e2020JD033484.
1016 <https://doi.org/10.1029/2020JD033484>
- 1017 Canagaratna, M. R., Jayne, J. T., Jimenez, J. L., Allan, J. D., Alfarra, M. R., Zhang, Q., et al.
1018 (2007). Chemical and microphysical characterization of ambient aerosols with the
1019 aerodyne aerosol mass spectrometer. *Mass Spectrometry Reviews*, 26(2), 185–222.
1020 <https://doi.org/10.1002/mas.20115>
- 1021 Chen, J., Wenger, J. C., & Venables, D. S. (2011). Near-Ultraviolet Absorption Cross Sections
1022 of Nitrophenols and Their Potential Influence on Tropospheric Oxidation Capacity.
1023 *The Journal of Physical Chemistry A*, 115(44), 12235–12242.
1024 <https://doi.org/10.1021/jp206929r>
- 1025 Collier, S., Zhou, S., Onasch, T. B., Jaffe, D. A., Kleinman, L., Sedlacek, A. J., et al. (2016).
1026 Regional Influence of Aerosol Emissions from Wildfires Driven by Combustion
1027 Efficiency: Insights from the BBOP Campaign. *Environmental Science & Technology*,
1028 50(16), 8613–8622. <https://doi.org/10.1021/acs.est.6b01617>
- 1029 Crilley, L. R., Kramer, L. J., Ouyang, B., Duan, J., Zhang, W., Tong, S., et al. (2019).
1030 Intercomparison of nitrous acid (HONO) measurement techniques in a megacity
1031 (Beijing). *Atmospheric Measurement Techniques*, 12(12), 6449–6463.
1032 <https://doi.org/10.5194/amt-12-6449-2019>
- 1033 Crounse, J. D., McKinney, K. A., Kwan, A. J., & Wennberg, P. O. (2006). Measurement of Gas-
1034 Phase Hydroperoxides by Chemical Ionization Mass Spectrometry. *Analytical*
1035 *Chemistry*, 78(19), 6726–6732. <https://doi.org/10.1021/ac0604235>



- 1036 Crutzen, P. J., & Andreae, M. O. (2016). Biomass Burning in the Tropics: Impact on
1037 Atmospheric Chemistry and Biogeochemical Cycles. In P. J. Crutzen & H. G. Brauch
1038 (Eds.), *Paul J. Crutzen: A Pioneer on Atmospheric Chemistry and Climate Change in*
1039 *the Anthropocene* (pp. 165–188). Cham: Springer International Publishing.
1040 https://doi.org/10.1007/978-3-319-27460-7_7
- 1041 Day, D. A., Dillon, M. B., Wooldridge, P. J., Thornton, J. A., Rosen, R. S., Wood, E. C., &
1042 Cohen, R. C. (2003). On alkyl nitrates, O₃, and the “missing NO_y.” *Journal of*
1043 *Geophysical Research: Atmospheres*, 108(D16).
1044 <https://doi.org/10.1029/2003JD003685>
- 1045 Day, D. A., Campuzano-Jost, P., Nault, B. A., Palm, B. B., Hu, W., Guo, H., et al. (2021). A
1046 Systematic Re-evaluation of Methods for Quantification of Bulk Particle-phase
1047 Organic Nitrates Using Real-time Aerosol Mass Spectrometry. *Atmospheric*
1048 *Measurement Techniques Discussions*, 1–35. <https://doi.org/10.5194/amt-2021-263>
- 1049 DeCarlo, P. F., Kimmel, J. R., Trimborn, A., Northway, M. J., Jayne, J. T., Aiken, A. C., et al.
1050 (2006). Field-Deployable, High-Resolution, Time-of-Flight Aerosol Mass
1051 Spectrometer. *Analytical Chemistry*, 78(24), 8281–8289.
1052 <https://doi.org/10.1021/ac061249n>
- 1053 Decker, Z. C. J., Robinson, M. A., Barsanti, K. C., Bourgeois, I., Coggon, M. M., DiGangi, J. P.,
1054 et al. (2021). Nighttime and Daytime Dark Oxidation Chemistry in Wildfire Plumes:
1055 An Observation and Model Analysis of FIREX-AQ Aircraft Data. *Atmospheric*
1056 *Chemistry and Physics Discussions*, 1–45. <https://doi.org/10.5194/acp-2021-267>
- 1057 Dennis, A., Fraser, M., Anderson, S., & Allen, D. (2002). Air pollutant emissions associated
1058 with forest, grassland, and agricultural burning in Texas. *Atmospheric Environment*,
1059 36(23), 3779–3792. [https://doi.org/10.1016/S1352-2310\(02\)00219-4](https://doi.org/10.1016/S1352-2310(02)00219-4)
- 1060 Diskin, G. S., Podolske, J. R., Sachse, G. W., & Slate, T. A. (2002). Open-path airborne tunable
1061 diode laser hygrometer. In *Diode Lasers and Applications in Atmospheric Sensing*
1062 (Vol. 4817, pp. 196–204). International Society for Optics and Photonics.
1063 <https://doi.org/10.1117/12.453736>
- 1064 Eisele, F. L., Mauldin, L., Cantrell, C., Zondlo, M., Apel, E., Fried, A., et al. (2003). Summary of
1065 measurement intercomparisons during TRACE-P. *Journal of Geophysical Research:*
1066 *Atmospheres*, 108(D20). <https://doi.org/10.1029/2002JD003167>
- 1067 Fahey, D. W., Eubank, C. S., Hübler, G., & Fehsenfeld, F. C. (1985). Evaluation of a catalytic
1068 reduction technique for the measurement of total reactive odd-nitrogen NO_y in the
1069 atmosphere. *Journal of Atmospheric Chemistry*, 3(4), 435–468.
- 1070 Fahey, D. W., Hübler, G., Parrish, D. D., Williams, E. J., Norton, R. B., Ridley, B. A., et al.
1071 (1986). Reactive nitrogen species in the troposphere: Measurements of NO, NO₂,
1072 HNO₃, particulate nitrate, peroxyacetyl nitrate (PAN), O₃, and total reactive odd
1073 nitrogen (NO_y) at Niwot Ridge, Colorado. *Journal of Geophysical Research:*
1074 *Atmospheres*, 91(D9), 9781–9793. <https://doi.org/10.1029/JD091iD09p09781>
- 1075 Farmer, D. K., Matsunaga, A., Docherty, K. S., Surratt, J. D., Seinfeld, J. H., Ziemann, P. J., &
1076 Jimenez, J. L. (2010). Response of an aerosol mass spectrometer to organonitrates
1077 and organosulfates and implications for atmospheric chemistry. *Proceedings of the*
1078 *National Academy of Sciences*, 107(15), 6670–6675.
1079 <https://doi.org/10.1073/pnas.0912340107>
- 1080 Fiedler, S. E., Hese, A., & Ruth, A. A. (2003). Incoherent broad-band cavity-enhanced
1081 absorption spectroscopy. *Chemical Physics Letters*, 371(3), 284–294.
1082 [https://doi.org/10.1016/S0009-2614\(03\)00263-X](https://doi.org/10.1016/S0009-2614(03)00263-X)



- 1083 Fisher, J. A., Jacob, D. J., Travis, K. R., Kim, P. S., Marais, E. A., Chan Miller, C., et al. (2016).
1084 Organic nitrate chemistry and its implications for nitrogen budgets in an isoprene-
1085 and monoterpene-rich atmosphere: constraints from aircraft (SEAC⁴RS) and ground-
1086 based (SOAS) observations in the Southeast US. *Atmospheric Chemistry and Physics*,
1087 *16*(9), 5969–5991. <https://doi.org/10.5194/acp-16-5969-2016>
1088 Fontijn, Arthur., Sabadell, A. J., & Ronco, R. J. (1970). Homogeneous chemiluminescent
1089 measurement of nitric oxide with ozone. Implications for continuous selective
1090 monitoring of gaseous air pollutants. *Analytical Chemistry*, *42*(6), 575–579.
1091 <https://doi.org/10.1021/ac60288a034>
1092 Fry, J. L., Draper, D. C., Zarzana, K. J., Campuzano-Jost, P., Day, D. A., Jimenez, J. L., et al.
1093 (2013). Observations of gas- and aerosol-phase organic nitrates at BEACHON-
1094 RoMBAS 2011. *Atmospheric Chemistry and Physics*, *13*(17), 8585–8605.
1095 <https://doi.org/10.5194/acp-13-8585-2013>
1096 Galloway, J. N., Aber, J. D., Erisman, J. W., Seitzinger, S. P., Howarth, R. W., Cowling, E. B., &
1097 Cosby, B. J. (2003). The Nitrogen Cascade. *BioScience*, *53*(4), 341.
1098 [https://doi.org/10.1641/0006-3568\(2003\)053\[0341:TNC\]2.0.CO;2](https://doi.org/10.1641/0006-3568(2003)053[0341:TNC]2.0.CO;2)
1099 Gao, R. S., McLaughlin, R. J., Schein, M. E., Neuman, J. A., Ciciora, S. J., Holecek, J. C., &
1100 Fahey, D. W. (1999). Computer-controlled Teflon flow control valve. *Review of*
1101 *Scientific Instruments*, *70*(12), 4732–4733. <https://doi.org/10.1063/1.1150137>
1102 Gregory, G. L., Hoell, J. M., Torres, A. L., Carroll, M. A., Ridley, B. A., Rodgers, M. O., et al.
1103 (1990). An intercomparison of airborne nitric oxide measurements: A second
1104 opportunity. *Journal of Geophysical Research: Atmospheres*, *95*(D7), 10129–10138.
1105 <https://doi.org/10.1029/JD095iD07p10129>
1106 Gregory, G. L., Hoell, J. M., Carroll, M. A., Ridley, B. A., Davis, D. D., Bradshaw, J., et al.
1107 (1990). An intercomparison of airborne nitrogen dioxide instruments. *Journal of*
1108 *Geophysical Research: Atmospheres*, *95*(D7), 10103–10127.
1109 <https://doi.org/10.1029/JD095iD07p10103>
1110 Guo, H., Campuzano-Jost, P., Pagonis, D., Schueneman, M., Day, D. A., Nault, B. A., et al.
1111 (2020). Submicron Particle Composition and Acidity in Fire Plumes during FIREX-AQ
1112 aircraft study, 2020, A232-10. Presented at the AGU Fall Meeting Abstracts.
1113 Guo, Hongyu, Campuzano-Jost, P., Nault, B. A., Day, D. A., Schroder, J. C., Kim, D., et al.
1114 (2021). The importance of size ranges in aerosol instrument intercomparisons: a case
1115 study for the Atmospheric Tomography Mission. *Atmospheric Measurement*
1116 *Techniques*, *14*(5), 3631–3655. <https://doi.org/10.5194/amt-14-3631-2021>
1117 Hall, B. D., Dutton, G. S., & Elkins, J. W. (2007). The NOAA nitrous oxide standard scale for
1118 atmospheric observations. *Journal of Geophysical Research: Atmospheres*, *112*(D9).
1119 <https://doi.org/10.1029/2006JD007954>
1120 Harder, J. W., & Brault, J. W. (1997). Atmospheric measurements of water vapor in the 442-
1121 nm region. *Journal of Geophysical Research: Atmospheres*, *102*(D5), 6245–6252.
1122 <https://doi.org/10.1029/96JD01730>
1123 Hayden, K. L., Anlauf, K. G., Hastie, D. R., & Bottenheim, J. W. (2003). Partitioning of reactive
1124 atmospheric nitrogen oxides at an elevated site in southern Quebec, Canada. *Journal*
1125 *of Geophysical Research: Atmospheres*, *108*(D19).
1126 <https://doi.org/10.1029/2002JD003188>
1127 Hoell, J. M., Gregory, G. L., McDougal, D. S., Sachse, G. W., Hill, G. F., Condon, E. P., &
1128 Rasmussen, R. A. (1987). Airborne intercomparison of carbon monoxide



- 1129 measurement techniques. *Journal of Geophysical Research: Atmospheres*, 92(D2),
1130 2009–2019. <https://doi.org/10.1029/JD092iD02p02009>
- 1131 Hoell, J. M., Gregory, G. L., McDougal, D. S., Torres, A. L., Davis, D. D., Bradshaw, J., et al.
1132 (1987). Airborne intercomparison of nitric oxide measurement techniques. *Journal of*
1133 *Geophysical Research: Atmospheres*, 92(D2), 1995–2008.
1134 <https://doi.org/10.1029/JD092iD02p01995>
- 1135 Holloway, J. S., Jakoubek, R. O., Parrish, D. D., Gerbig, C., Volz-Thomas, A., Schmitgen, S., et
1136 al. (2000). Airborne intercomparison of vacuum ultraviolet fluorescence and tunable
1137 diode laser absorption measurements of tropospheric carbon monoxide. *Journal of*
1138 *Geophysical Research: Atmospheres*, 105(D19), 24251–24261.
1139 <https://doi.org/10.1029/2000JD900237>
- 1140 Holmes, C. D., Fite, C., Agastra, A., Schwarz, J. P., Yokelson, R. J., Bui, T. V., & Peterson, D. A.
1141 (2020). Critical evaluation of smoke age inferred from different methods during
1142 FIREX-AQ, 2020, A225-0010. Presented at the AGU Fall Meeting Abstracts.
- 1143 Jaffe, D. A., O’Neill, S. M., Larkin, N. K., Holder, A. L., Peterson, D. L., Halofsky, J. E., &
1144 Rappold, A. G. (2020). Wildfire and prescribed burning impacts on air quality in the
1145 United States. *Journal of the Air & Waste Management Association*, 70(6), 583–615.
1146 <https://doi.org/10.1080/10962247.2020.1749731>
- 1147 Johnston, F. H., Henderson Sarah B., Chen Yang, Randerson James T., Marlier Miriam,
1148 DeFries Ruth S., et al. (2012). Estimated Global Mortality Attributable to Smoke from
1149 Landscape Fires. *Environmental Health Perspectives*, 120(5), 695–701.
1150 <https://doi.org/10.1289/ehp.1104422>
- 1151 Johnston, F. H., Borchers-Arriagada, N., Morgan, G. G., Jalaludin, B., Palmer, A. J.,
1152 Williamson, G. J., & Bowman, D. M. J. S. (2021). Unprecedented health costs of
1153 smoke-related PM_{2.5} from the 2019–20 Australian megafires. *Nature Sustainability*,
1154 4(1), 42–47. <https://doi.org/10.1038/s41893-020-00610-5>
- 1155 Keller-Rudek, H., Moortgat, G. K., Sander, R., & Sørensen, R. (2013). The MPI-Mainz UV/VIS
1156 Spectral Atlas of Gaseous Molecules of Atmospheric Interest. *Earth System Science*
1157 *Data*, 5(2), 365–373. <https://doi.org/10.5194/essd-5-365-2013>
- 1158 Kleffmann, J., Lörzer, J. C., Wiesen, P., Kern, C., Trick, S., Volkamer, R., et al. (2006).
1159 Intercomparison of the DOAS and LOPAP techniques for the detection of nitrous acid
1160 (HONO). *Atmospheric Environment*, 40(20), 3640–3652.
1161 <https://doi.org/10.1016/j.atmosenv.2006.03.027>
- 1162 Kleffmann, Jörg. (2007). Daytime Sources of Nitrous Acid (HONO) in the Atmospheric
1163 Boundary Layer. *ChemPhysChem*, 8(8), 1137–1144.
1164 <https://doi.org/10.1002/cphc.200700016>
- 1165 Kroll, J. H., & Seinfeld, J. H. (2008). Chemistry of secondary organic aerosol: Formation and
1166 evolution of low-volatility organics in the atmosphere. *Atmospheric Environment*,
1167 42(16), 3593–3624. <https://doi.org/10.1016/j.atmosenv.2008.01.003>
- 1168 Lao, M., Crilley, L. R., Salehpoor, L., Furlani, T. C., Bourgeois, I., Neuman, J. A., et al. (2020). A
1169 portable, robust, stable, and tunable calibration source for gas-phase nitrous acid
1170 (HONO). *Atmospheric Measurement Techniques*, 13(11), 5873–5890.
1171 <https://doi.org/10.5194/amt-13-5873-2020>
- 1172 Lareau, N. P., Nauslar, N. J., & Abatzoglou, J. T. (2018). The Carr Fire Vortex: A Case of
1173 Pyrotornadogenesis? *Geophysical Research Letters*, 45(23), 13,107–13,115.
1174 <https://doi.org/10.1029/2018GL080667>



- 1175 Lee, B. H., Lopez-Hilfiker, F. D., Mohr, C., Kurtén, T., Worsnop, D. R., & Thornton, J. A. (2014).
1176 An Iodide-Adduct High-Resolution Time-of-Flight Chemical-Ionization Mass
1177 Spectrometer: Application to Atmospheric Inorganic and Organic Compounds.
1178 *Environmental Science & Technology*, 48(11), 6309–6317.
1179 <https://doi.org/10.1021/es500362a>
- 1180 Lee, Y. R., Ji, Y., Tanner, D. J., & Huey, L. G. (2020). A low-activity ion source for
1181 measurement of atmospheric gases by chemical ionization mass spectrometry.
1182 *Atmospheric Measurement Techniques*, 13(5), 2473–2480.
1183 <https://doi.org/10.5194/amt-13-2473-2020>
- 1184 Lerner, B. M., Gilman, J. B., Aikin, K. C., Atlas, E. L., Goldan, P. D., Graus, M., et al. (2017). An
1185 improved, automated whole air sampler and gas chromatography mass
1186 spectrometry analysis system for volatile organic compounds in the atmosphere.
1187 *Atmospheric Measurement Techniques*, 10(1), 291–313.
1188 <https://doi.org/10.5194/amt-10-291-2017>
- 1189 Liousse, C., Guillaume, B., Grégoire, J. M., Mallet, M., Galy, C., Pont, V., et al. (2010).
1190 Updated African biomass burning emission inventories in the framework of the
1191 AMMA-IDAF program, with an evaluation of combustion aerosols. *Atmospheric
1192 Chemistry and Physics*, 10(19), 9631–9646. [https://doi.org/10.5194/acp-10-9631-
1193 2010](https://doi.org/10.5194/acp-10-9631-2010)
- 1194 McCarty, J. L. (2011). Remote Sensing-Based Estimates of Annual and Seasonal Emissions
1195 from Crop Residue Burning in the Contiguous United States. *Journal of the Air &
1196 Waste Management Association*, 61(1), 22–34. [https://doi.org/10.3155/1047-
1197 3289.61.1.22](https://doi.org/10.3155/1047-3289.61.1.22)
- 1198 Meller, R., Raber, W., Crowley, J. N., Jenkin, M. E., & Moortgat, G. K. (1991). The UV-visible
1199 absorption spectrum of methylglyoxal. *Journal of Photochemistry and Photobiology
1200 A: Chemistry*, 62(2), 163–171. [https://doi.org/10.1016/1010-6030\(91\)87017-P](https://doi.org/10.1016/1010-6030(91)87017-P)
- 1201 Melvin, M. A. (2020). *2020 National Prescribed Fire Use Report*. National Association of State
1202 Foresters. Retrieved from [https://www.stateforesters.org/wp-
1203 content/uploads/2020/12/2020-Prescribed-Fire-Use-Report.pdf](https://www.stateforesters.org/wp-content/uploads/2020/12/2020-Prescribed-Fire-Use-Report.pdf)
- 1204 Min, K.-E., Washenfelder, R. A., Dubé, W. P., Langford, A. O., Edwards, P. M., Zarzana, K. J.,
1205 et al. (2016). A broadband cavity enhanced absorption spectrometer for aircraft
1206 measurements of glyoxal, methylglyoxal, nitrous acid, nitrogen dioxide, and water
1207 vapor. *Atmospheric Measurement Techniques*, 9(2), 423–440.
1208 <https://doi.org/10.5194/amt-9-423-2016>
- 1209 Nault, B. A., Garland, C., Pusede, S. E., Wooldridge, P. J., Ullmann, K., Hall, S. R., & Cohen, R.
1210 C. (2015). Measurements of CH₃O₂NO₂ in the upper troposphere. *Atmospheric
1211 Measurement Techniques*, 8(2), 987–997. <https://doi.org/10.5194/amt-8-987-2015>
- 1212 Neuman, J. A., Trainer, M., Brown, S. S., Min, K.-E., Nowak, J. B., Parrish, D. D., et al. (2016).
1213 HONO emission and production determined from airborne measurements over the
1214 Southeast U.S. *Journal of Geophysical Research: Atmospheres*, 121(15),
1215 2016JD025197. <https://doi.org/10.1002/2016JD025197>
- 1216 Ninneman, M., Marto, J., Shaw, S., Edgerton, E., Blanchard, C., & Schwab, J. (2021). Reactive
1217 oxidized nitrogen speciation and partitioning in urban and rural New York State.
1218 *Journal of the Air & Waste Management Association*, 71(3), 348–365.
1219 <https://doi.org/10.1080/10962247.2020.1837289>
- 1220 Novelli, P. C., Elkins, J. W., & Steele, L. P. (1991). The development and evaluation of a
1221 gravimetric reference scale for measurements of atmospheric carbon monoxide.



- 1222 *Journal of Geophysical Research: Atmospheres*, 96(D7), 13109–13121.
1223 <https://doi.org/10.1029/91JD01108>
- 1224 O’Dell, K., Ford, B., Fischer, E. V., & Pierce, J. R. (2019). Contribution of Wildland-Fire Smoke
1225 to US PM_{2.5} and Its Influence on Recent Trends. *Environmental Science &*
1226 *Technology*, 53(4), 1797–1804. <https://doi.org/10.1021/acs.est.8b05430>
- 1227 Pagonis, D., Campuzano-Jost, P., Guo, H., Day, D. A., Schueneman, M. K., Brown, W. L., et al.
1228 (2021). Airborne extractive electrospray mass spectrometry measurements of the
1229 chemical composition of organic aerosol. *Atmospheric Measurement Techniques*,
1230 14(2), 1545–1559. <https://doi.org/10.5194/amt-14-1545-2021>
- 1231 Peischl, J., Ryerson, T. B., Holloway, J. S., Parrish, D. D., Trainer, M., Frost, G. J., et al. (2010).
1232 A top-down analysis of emissions from selected Texas power plants during TexAQSt
1233 2000 and 2006. *Journal of Geophysical Research: Atmospheres*, 115(D16).
1234 <https://doi.org/10.1029/2009JD013527>
- 1235 Peng, Q., Palm, B. B., Melander, K. E., Lee, B. H., Hall, S. R., Ullmann, K., et al. (2020). HONO
1236 Emissions from Western U.S. Wildfires Provide Dominant Radical Source in Fresh
1237 Wildfire Smoke. *Environmental Science & Technology*.
1238 <https://doi.org/10.1021/acs.est.0c00126>
- 1239 Pinto, J. P., Dibb, J., Lee, B. H., Rappenglück, B., Wood, E. C., Levy, M., et al. (2014).
1240 Intercomparison of field measurements of nitrous acid (HONO) during the SHARP
1241 campaign. *Journal of Geophysical Research: Atmospheres*, 119(9), 5583–5601.
1242 <https://doi.org/10.1002/2013JD020287>
- 1243 Platt, U., Perner, D., Harris, G. W., Winer, A. M., & Pitts, J. N. (1980). Observations of nitrous
1244 acid in an urban atmosphere by differential optical absorption. *Nature*, 285(5763),
1245 312–314. <https://doi.org/10.1038/285312a0>
- 1246 Podolske, J. R., Sachse, G. W., & Diskin, G. S. (2003). Calibration and data retrieval
1247 algorithms for the NASA Langley/Ames Diode Laser Hygrometer for the NASA
1248 Transport and Chemical Evolution Over the Pacific (TRACE-P) mission. *Journal of*
1249 *Geophysical Research: Atmospheres*, 108(D20).
1250 <https://doi.org/10.1029/2002JD003156>
- 1251 Pollack, I. B., Homeyer, C. R., Ryerson, T. B., Aikin, K. C., Peischl, J., Apel, E. C., et al. (2016).
1252 Airborne quantification of upper tropospheric NO_x production from lightning in deep
1253 convective storms over the United States Great Plains. *Journal of Geophysical*
1254 *Research: Atmospheres*, 121(4), 2002–2028. <https://doi.org/10.1002/2015JD023941>
- 1255 Pollack, Ilana B., Lerner, B. M., & Ryerson, T. B. (2011). Evaluation of ultraviolet light-
1256 emitting diodes for detection of atmospheric NO₂ by photolysis -
1257 chemiluminescence. *Journal of Atmospheric Chemistry*, 65(2–3), 111–125.
1258 <https://doi.org/10.1007/s10874-011-9184-3>
- 1259 Ridley, B. A., & Grahek, F. E. (1990). A Small, Low Flow, High Sensitivity Reaction Vessel for
1260 NO Chemiluminescence Detectors. *Journal of Atmospheric and Oceanic Technology*,
1261 7(2), 307–311. [https://doi.org/10.1175/1520-0426\(1990\)007<0307:ASLFHS>2.0.CO;2](https://doi.org/10.1175/1520-0426(1990)007<0307:ASLFHS>2.0.CO;2)
- 1262 Ridley, B. A., & Howlett, L. C. (1974). An instrument for nitric oxide measurements in the
1263 stratosphere. *Review of Scientific Instruments*, 45(6), 742–746.
1264 <https://doi.org/10.1063/1.1686726>
- 1265 Ridley, B. A., Grahek, F. E., & Walega, J. G. (1992). A Small High-Sensitivity, Medium-
1266 Response Ozone Detector Suitable for Measurements from Light Aircraft. *Journal of*
1267 *Atmospheric and Oceanic Technology*, 9(2), 142–148. [https://doi.org/10.1175/1520-0426\(1992\)009<0142:ASHSMR>2.0.CO;2](https://doi.org/10.1175/1520-0426(1992)009<0142:ASHSMR>2.0.CO;2)
- 1268



- 1269 Roberts, J. M., Stockwell, C. E., Yokelson, R. J., de Gouw, J., Liu, Y., Selimovic, V., et al. (2020).
1270 The nitrogen budget of laboratory-simulated western US wildfires during the FIREX
1271 2016 Fire Lab study. *Atmospheric Chemistry and Physics*, 20(14), 8807–8826.
1272 <https://doi.org/10.5194/acp-20-8807-2020>
- 1273 Robinson, M. A., Decker, Z. C. J., Barsanti, K. C., Coggon, M. M., Flocke, F. M., Franchin, A., et
1274 al. (2021). Variability and Time of Day Dependence of Ozone Photochemistry in
1275 Western Wildfire Plumes. *Environmental Science & Technology*, 55(15), 10280–
1276 10290. <https://doi.org/10.1021/acs.est.1c01963>
- 1277 Rollins, A. W., Rickly, P. S., Gao, R.-S., Ryerson, T. B., Brown, S. S., Peischl, J., & Bourgeois, I.
1278 (2020). Single-photon laser-induced fluorescence detection of nitric oxide at sub-
1279 parts-per-trillion mixing ratios. *Atmospheric Measurement Techniques*, 13(5), 2425–
1280 2439. <https://doi.org/10.5194/amt-13-2425-2020>
- 1281 Russo, R. S., Zhou, Y., Haase, K. B., Wingenter, O. W., Frinak, E. K., Mao, H., et al. (2010).
1282 Temporal variability, sources, and sinks of C₁–C₅ alkyl nitrates in coastal New England.
1283 *Atmospheric Chemistry and Physics*, 10(4), 1865–1883. <https://doi.org/10.5194/acp-10-1865-2010>
- 1285 Ryerson, T. B., Huey, L. G., Knapp, K., Neuman, J. A., Parrish, D. D., Sueper, D. T., &
1286 Fehsenfeld, F. C. (1999). Design and initial characterization of an inlet for gas-phase
1287 NO_y measurements from aircraft. *Journal of Geophysical Research: Atmospheres*,
1288 104(D5), 5483–5492. <https://doi.org/10.1029/1998JD100087>
- 1289 Ryerson, T. B., Williams, E. J., & Fehsenfeld, F. C. (2000). An efficient photolysis system for
1290 fast-response NO₂ measurements. *Journal of Geophysical Research: Atmospheres*,
1291 105(D21), 26447–26461. <https://doi.org/10.1029/2000JD900389>
- 1292 Sachse, G. W., Hill, G. F., Wade, L. O., & Perry, M. G. (1987). Fast-response, high-precision
1293 carbon monoxide sensor using a tunable diode laser absorption technique. *Journal of*
1294 *Geophysical Research: Atmospheres*, 92(D2), 2071–2081.
1295 <https://doi.org/10.1029/JD092iD02p02071>
- 1296 Selimovic, V., Yokelson, R. J., Warneke, C., Roberts, J. M., de Gouw, J., Reardon, J., & Griffith,
1297 D. W. T. (2018). Aerosol optical properties and trace gas emissions by PAX and OP-
1298 FTIR for laboratory-simulated western US wildfires during FIREX. *Atmospheric*
1299 *Chemistry and Physics*, 18(4), 2929–2948. <https://doi.org/10.5194/acp-18-2929-2018>
- 1300 Slusher, D. L., Huey, L. G., Tanner, D. J., Flocke, F. M., & Roberts, J. M. (2004). A thermal
1301 dissociation–chemical ionization mass spectrometry (TD-CIMS) technique for the
1302 simultaneous measurement of peroxyacyl nitrates and dinitrogen pentoxide. *Journal*
1303 *of Geophysical Research: Atmospheres*, 109(D19).
1304 <https://doi.org/10.1029/2004JD004670>
- 1305 Sparks, T. L., Ebben, C. J., Wooldridge, P. J., Lopez-Hilfiker, F. D., Lee, B. H., Thornton, J. A., et
1306 al. (2019). Comparison of Airborne Reactive Nitrogen Measurements During
1307 WINTER. *Journal of Geophysical Research: Atmospheres*, 124(19), 10483–10502.
1308 <https://doi.org/10.1029/2019JD030700>
- 1309 St. Clair, J. M., Swanson, A. K., Bailey, S. A., & Hanisco, T. F. (2019). CAFE: a new, improved
1310 nonresonant laser-induced fluorescence instrument for airborne in situ
1311 measurement of formaldehyde. *Atmospheric Measurement Techniques*, 12(8), 4581–
1312 4590. <https://doi.org/10.5194/amt-12-4581-2019>
- 1313 Stein, A. F., Draxler, R. R., Rolph, G. D., Stunder, B. J. B., Cohen, M. D., & Ngan, F. (2015).
1314 NOAA’s HYSPLIT Atmospheric Transport and Dispersion Modeling System. *Bulletin of*



- 1315 *the American Meteorological Society*, 96(12), 2059–2077.
1316 <https://doi.org/10.1175/BAMS-D-14-00110.1>
- 1317 Stockwell, C. E., Yokelson, R. J., Kreidenweis, S. M., Robinson, A. L., DeMott, P. J., Sullivan, R.
1318 C., et al. (2014). Trace gas emissions from combustion of peat, crop residue,
1319 domestic biofuels, grasses, and other fuels: configuration and Fourier transform
1320 infrared (FTIR) component of the fourth Fire Lab at Missoula Experiment (FLAME-4).
1321 *Atmospheric Chemistry and Physics*, 14(18), 9727–9754.
1322 <https://doi.org/10.5194/acp-14-9727-2014>
- 1323 Stutz, J., Kim, E. S., Platt, U., Bruno, P., Perrino, C., & Febo, A. (2000). UV-visible absorption
1324 cross sections of nitrous acid. *Journal of Geophysical Research: Atmospheres*,
1325 105(D11), 14585–14592. <https://doi.org/10.1029/2000JD900003>
- 1326 Theys, N., Volkamer, R., Müller, J.-F., Zarzana, K. J., Kille, N., Clarisse, L., et al. (2020). Global
1327 nitrous acid emissions and levels of regional oxidants enhanced by wildfires. *Nature*
1328 *Geoscience*, 13(10), 681–686. <https://doi.org/10.1038/s41561-020-0637-7>
- 1329 Vandaele, A. C., Hermans, C., Simon, P. C., Carleer, M., Colin, R., Fally, S., et al. (1998).
1330 Measurements of the NO₂ absorption cross-section from 42 000 cm⁻¹ to 10 000
1331 cm⁻¹ (238–1000 nm) at 220 K and 294 K. *Journal of Quantitative Spectroscopy and*
1332 *Radiative Transfer*, 59(3), 171–184. [https://doi.org/10.1016/S0022-4073\(97\)00168-4](https://doi.org/10.1016/S0022-4073(97)00168-4)
- 1333 Veres, P. R., Neuman, J. A., Bertram, T. H., Assaf, E., Wolfe, G. M., Williamson, C. J., et al.
1334 (2020). Global airborne sampling reveals a previously unobserved dimethyl sulfide
1335 oxidation mechanism in the marine atmosphere. *Proceedings of the National*
1336 *Academy of Sciences*, 117(9), 4505–4510. <https://doi.org/10.1073/pnas.1919344117>
- 1337 Volkamer, R., Molina, L. T., Molina, M. J., Shirley, T., & Brune, W. H. (2005). DOAS
1338 measurement of glyoxal as an indicator for fast VOC chemistry in urban air.
1339 *Geophysical Research Letters*, 32(8). <https://doi.org/10.1029/2005GL022616>
- 1340 Volpe Horii, C., William Munger, J., Wofsy, S. C., Zahniser, M., Nelson, D., & Barry McManus,
1341 J. (2005). Atmospheric reactive nitrogen concentration and flux budgets at a
1342 Northeastern U.S. forest site. *Agricultural and Forest Meteorology*, 133(1), 210–225.
1343 <https://doi.org/10.1016/j.agrformet.2004.08.009>
- 1344 Warneke, C., Trainer, M., Gouw, J. A. de, Parrish, D. D., Fahey, D. W., Ravishankara, A. R., et
1345 al. (2016). Instrumentation and measurement strategy for the NOAA SENEX aircraft
1346 campaign as part of the Southeast Atmosphere Study 2013. *Atmospheric*
1347 *Measurement Techniques*, 9(7), 3063–3093. [https://doi.org/10.5194/amt-9-3063-](https://doi.org/10.5194/amt-9-3063-2016)
1348 2016
- 1349 Washenfelder, R. A., Langford, A. O., Fuchs, H., & Brown, S. S. (2008). Measurement of
1350 glyoxal using an incoherent broadband cavity enhanced absorption spectrometer.
1351 *Atmospheric Chemistry and Physics*, 8(24), 7779–7793. [https://doi.org/10.5194/acp-](https://doi.org/10.5194/acp-8-7779-2008)
1352 8-7779-2008
- 1353 von der Weiden, S.-L., Drewnick, F., & Borrmann, S. (2009). Particle Loss Calculator – a new
1354 software tool for the assessment of the performance of aerosol inlet systems.
1355 *Atmospheric Measurement Techniques*, 2(2), 479–494. [https://doi.org/10.5194/amt-](https://doi.org/10.5194/amt-2-479-2009)
1356 2-479-2009
- 1357 van der Werf, G. R., Randerson, J. T., Giglio, L., Collatz, G. J., Mu, M., Kasibhatla, P. S., et al.
1358 (2010). Global fire emissions and the contribution of deforestation, savanna, forest,
1359 agricultural, and peat fires (1997–2009). *Atmospheric Chemistry and Physics*, 10(23),
1360 11707–11735. <https://doi.org/10.5194/acp-10-11707-2010>



- 1361 van der Werf, G. R., Randerson, J. T., Giglio, L., van Leeuwen, T. T., Chen, Y., Rogers, B. M., et
1362 al. (2017). Global fire emissions estimates during 1997–2016. *Earth System Science*
1363 *Data*, 9(2), 697–720. <https://doi.org/10.5194/essd-9-697-2017>
- 1364 Westerling, A. L. (2016). Increasing western US forest wildfire activity: sensitivity to changes
1365 in the timing of spring. *Philosophical Transactions of the Royal Society B: Biological*
1366 *Sciences*, 371(1696), 20150178. <https://doi.org/10.1098/rstb.2015.0178>
- 1367 Williams, E. J., Roberts, J. M., Baumann, K., Bertman, S. B., Buhr, S., Norton, R. B., &
1368 Fehsenfeld, F. C. (1997). Variations in NO_y composition at Idaho Hill, Colorado.
1369 *Journal of Geophysical Research: Atmospheres*, 102(D5), 6297–6314.
1370 <https://doi.org/10.1029/96JD03252>
- 1371 Womack, C. C., Neuman, J. A., Veres, P. R., Eilerman, S. J., Brock, C. A., Decker, Z. C. J., et al.
1372 (2017). Evaluation of the accuracy of thermal dissociation CRDS and LIF techniques
1373 for atmospheric measurement of reactive nitrogen species. *Atmos. Meas. Tech.*,
1374 10(5), 1911–1926. <https://doi.org/10.5194/amt-10-1911-2017>
- 1375 Wotawa, G. (2000). The Influence of Canadian Forest Fires on Pollutant Concentrations in
1376 the United States. *Science*, 288(5464), 324–328.
1377 <https://doi.org/10.1126/science.288.5464.324>
- 1378 Xu, L., Crouse, J. D., Vasquez, K., Allen, H. M., Wennberg, P. O., Bourgeois, I., et al. (2021).
1379 Ozone chemistry in Western U.S. wildfire plumes. *Science Advances*, *in press*.
- 1380 Xu, Z., Liu, Y., Nie, W., Sun, P., Chi, X., & Ding, A. (2019). Evaluating the measurement
1381 interference of wet rotating-denuder-ion chromatography in measuring
1382 atmospheric HONO in a highly polluted area. *Atmospheric Measurement Techniques*,
1383 12(12), 6737–6748. <https://doi.org/10.5194/amt-12-6737-2019>
- 1384 Yokelson, R. J., Griffith, D. W. T., & Ward, D. E. (1996). Open-path Fourier transform infrared
1385 studies of large-scale laboratory biomass fires. *Journal of Geophysical Research:*
1386 *Atmospheres*, 101(D15), 21067–21080. <https://doi.org/10.1029/96JD01800>
- 1387 Zhang, L., Wiebe, A., Vet, R., Mihele, C., O'Brien, J. M., Iqbal, S., & Liang, Z. (2008).
1388 Measurements of reactive oxidized nitrogen at eight Canadian rural sites.
1389 *Atmospheric Environment*, 42(34), 8065–8078.
1390 <https://doi.org/10.1016/j.atmosenv.2008.06.034>
- 1391 Ziemann, P. J., & Atkinson, R. (2012). Kinetics, products, and mechanisms of secondary
1392 organic aerosol formation. *Chemical Society Reviews*, 41(19), 6582–6605.
1393 <https://doi.org/10.1039/C2CS35122F>
- 1394

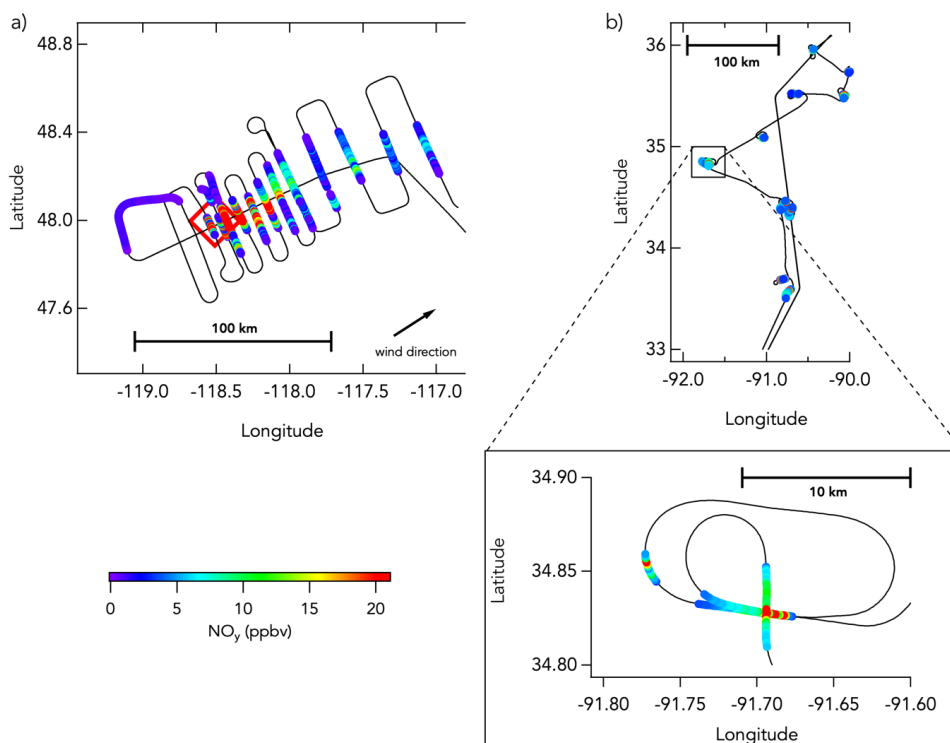


Figure 1 Examples DC-8 flight tracks from western wildfires and eastern agricultural fires. Panel a) shows the DC-8 flight track (black line) during the sampling of the Williams Flat fire (03/08/2019) smoke plume, colored by NO_y mixing ratios (only data in smoke are colored here). Panel b) shows the DC-8 flight track during the sampling of multiple agricultural burns (21/08/2019), also colored by NO_y mixing ratios (only data in smoke are colored here).

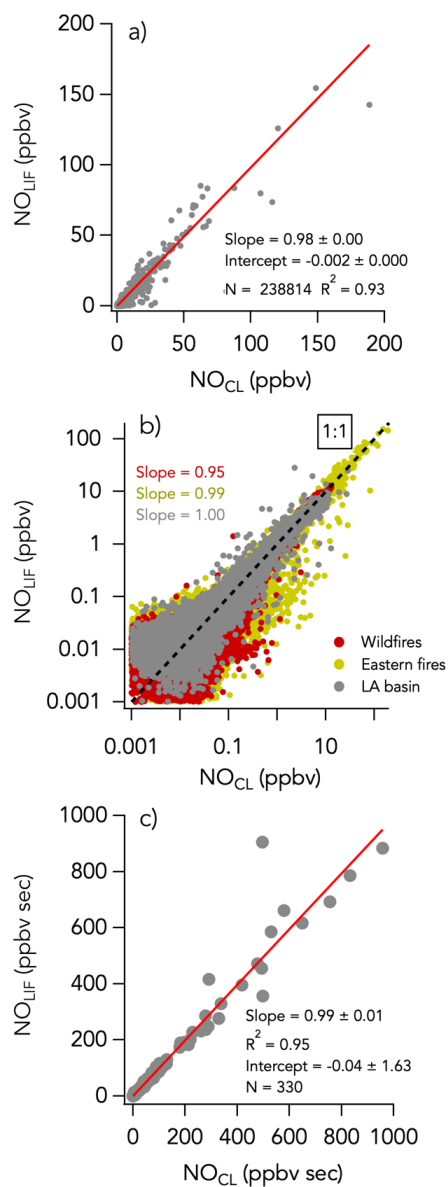


Figure 2 NO measurements by LIF versus CL with a) 1 s data on a linear scale, b) 1 s data on a log scale, and c) integrals of 330 crosswind smoke plume transects. N is the number of independent 1 s observations or smoke plume transects that are compared. In panel b, the three sampling periods are shown in different colors with the wildfires sampling period in red, the eastern fires sampling period in mustard, and the Los Angeles (LA) Basin flights in grey. The red lines indicate the fit of the data. The dotted black line is the 1:1 line.

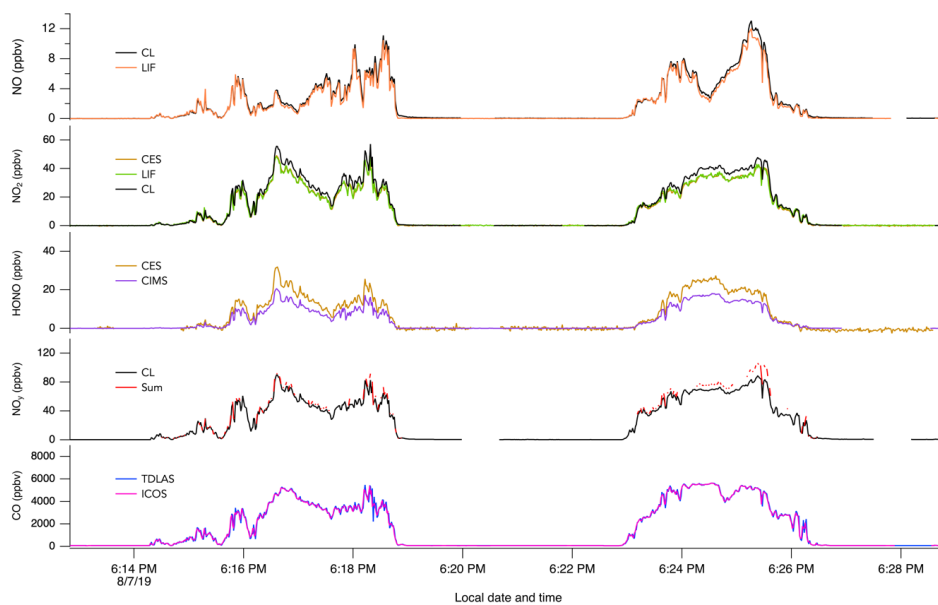


Figure 3 1 s measurements of a) NO, b) NO₂, c) HONO, d) NO_y, and e) CO during two crosswind plume transects of smoke from the Williams Flat fire on 07/08/2019. The plume transects were chosen due to the significant enhancement of all species at that time. Note that in panel b) the NO₂ trace from the CES instrument is hidden behind the NO₂ trace from the LIF instrument.

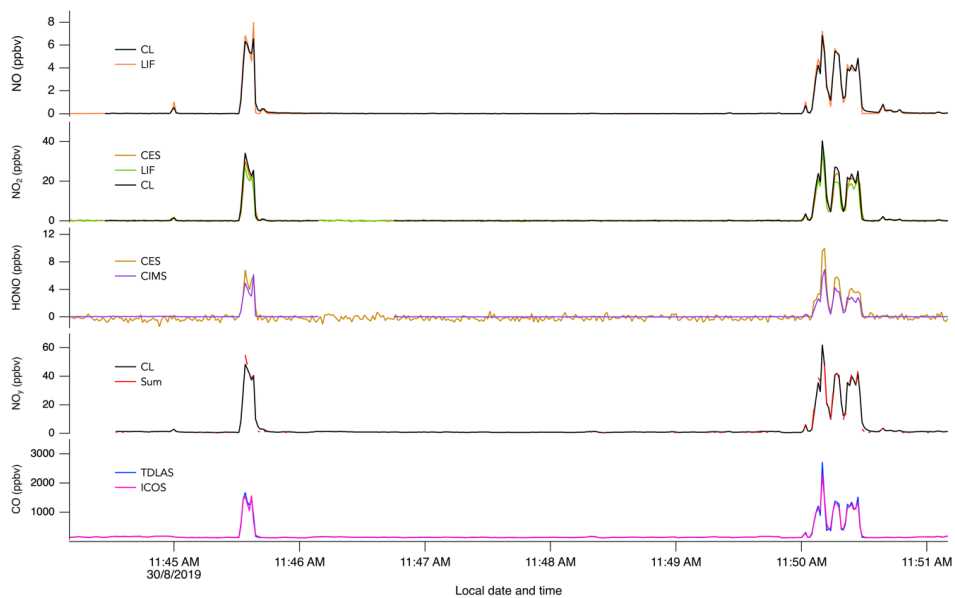


Figure 4 1 s measurements of a) NO, b) NO₂, c) HONO, d) NO_y, and e) CO during crosswind plume transects of smoke from crop burning in southeastern US on 30/08/2019.

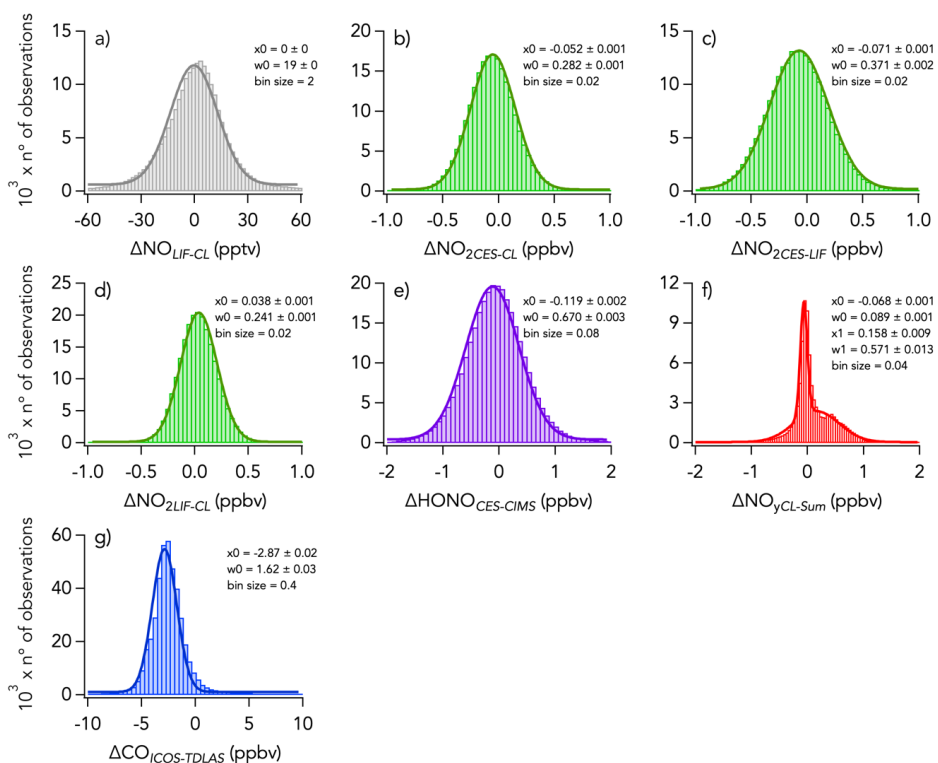


Figure 5 Histograms of the absolute difference of 1 s measurements of a) NO, b)–d) NO₂, e) HONO, f) NO_y, g) CO for the entire campaign. Parameters of the gaussian fit to the histogram is indicated in each panel with x0 and w0 being the central value and the width of the fit, respectively. Note that in panel f) a double gaussian was fitted to the histogram and that the parameters for the second mode are given by x1 and w1.

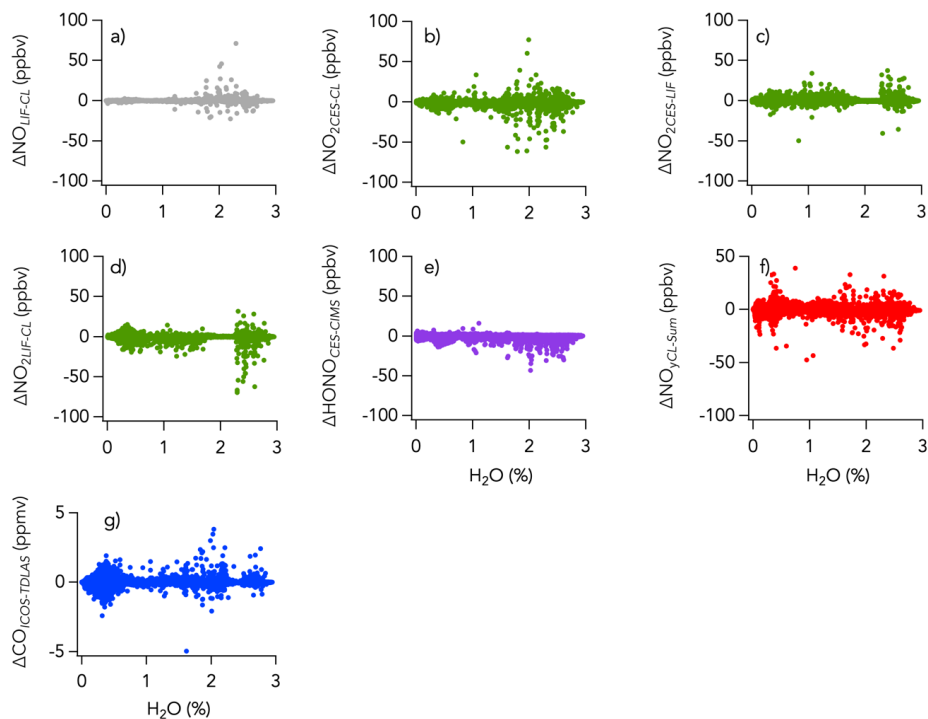


Figure 6 Measurement difference (1 s data) of a) NO, b)–d) NO₂, e) HONO, f) NO_y, g) CO as a function of water vapor for the entire campaign.

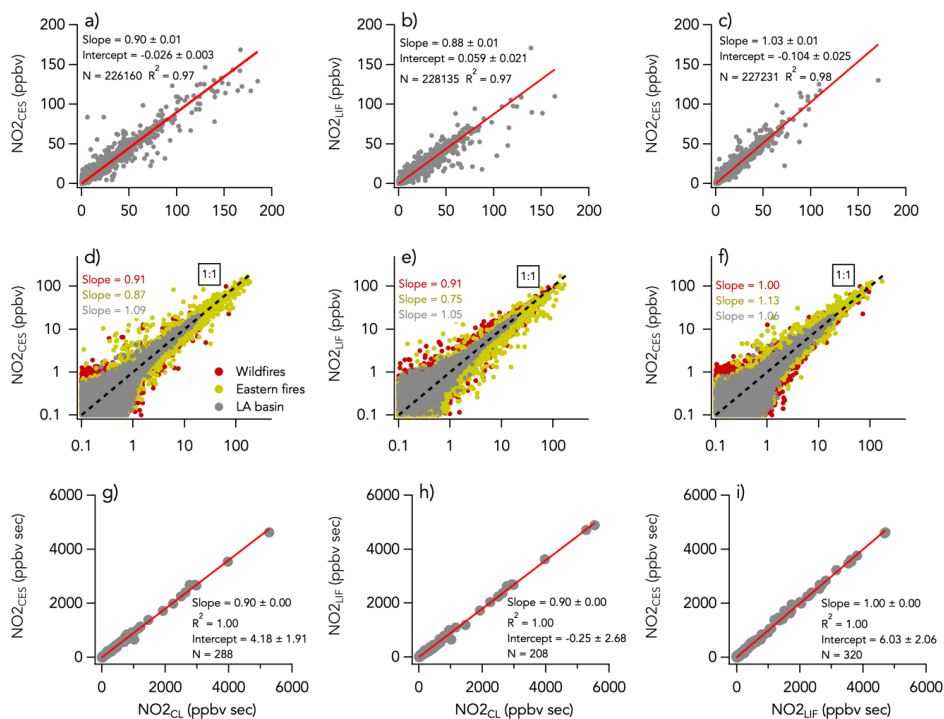


Figure 7 NO₂ measurements by LIF, CES and CL with a)–c) 1 s data on a linear scale, d)–f) 1 s data on a log scale, and g)–i) integrals of 208–320 crosswind smoke plume transects. N is the number of independent 1 s observations or smoke plume transects that are compared. In the panels d)–f), the three sampling periods are shown in different colors with the wildfires sampling period in red, the eastern fires sampling period in mustard, and the Los Angeles (LA) Basin flights in grey. The red lines indicate the fit of the data. The dotted black lines are the 1:1 line.

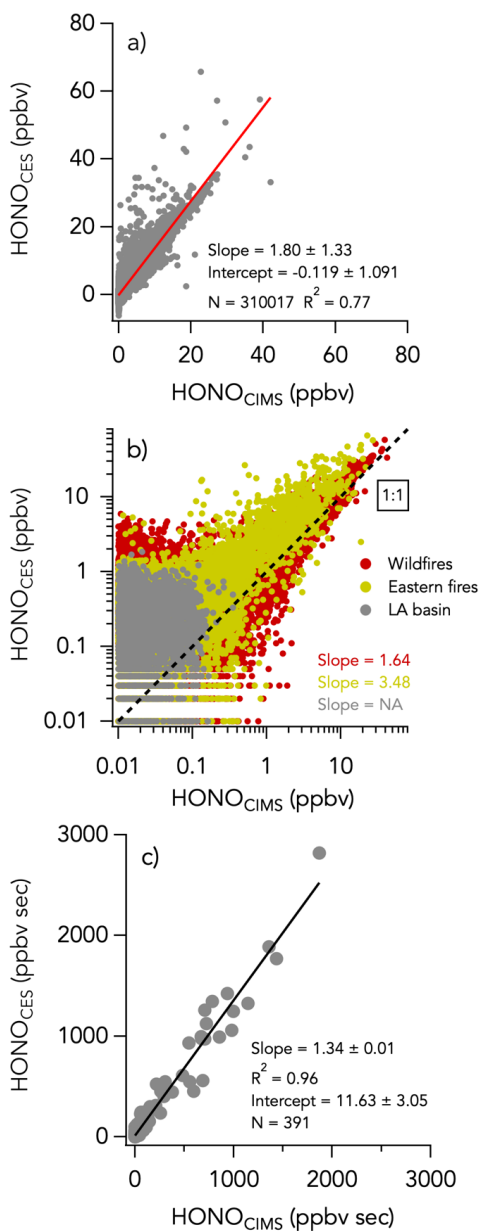


Figure 8 Same as Figure 2 but comparing HONO measurements by CES and CIMS. No slope is given for the Los Angeles (LA) flights in panel as most of the HONO signal at that time was below the instruments' detection limits.

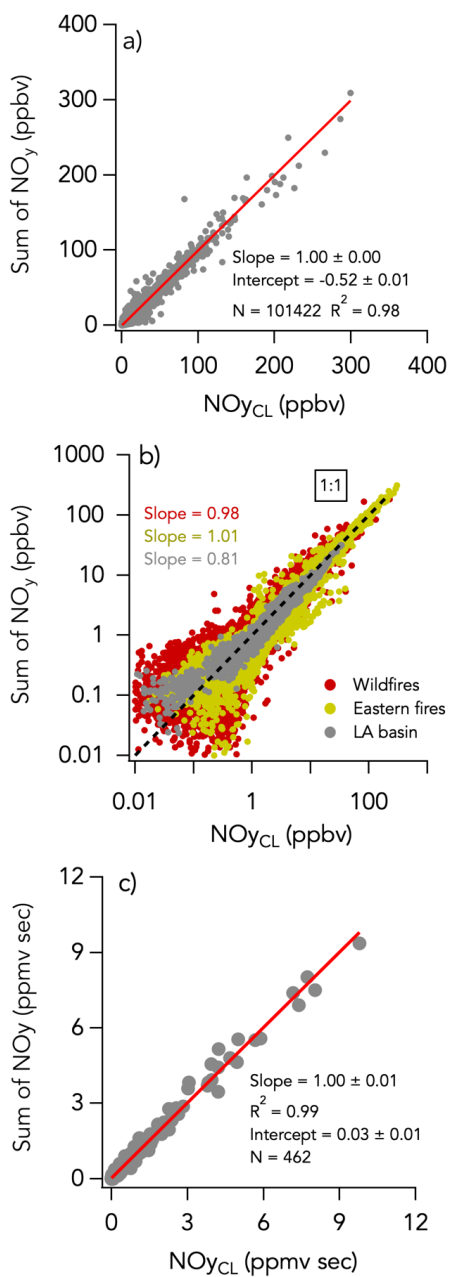


Figure 9 Same as Figure 2 but comparing the sum of individually measured NO_y species (= $\text{NO}_x + \text{HONO} + \text{HNO}_3 + \text{APNs} + \text{pNO}_3$) with the total NO_y measurement by CL.

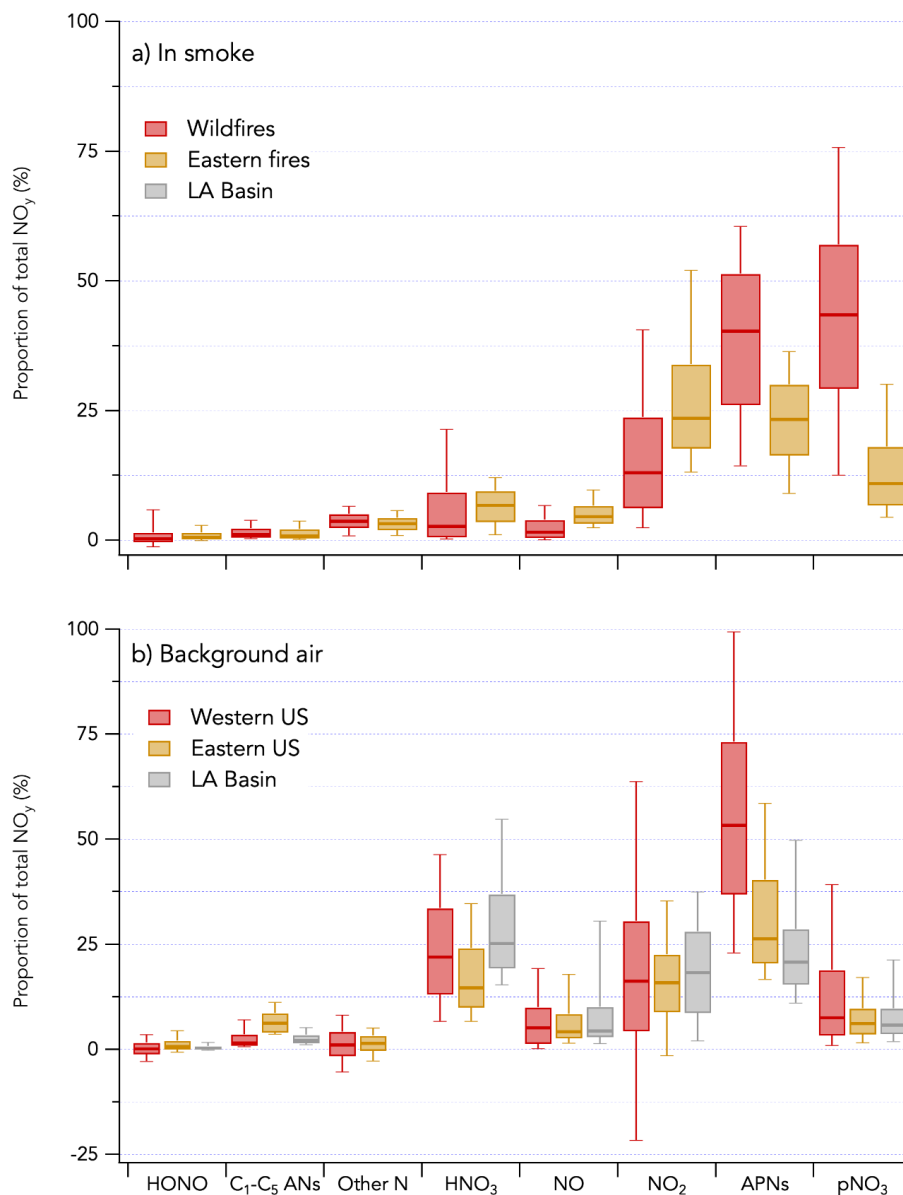


Figure 10 Contribution of individually measured reactive odd nitrogen species to the total NO_y budget during FIREX-AQ. The campaign is separated in three periods (wildfires sampling period in red, eastern fires sampling period in yellow, and Los Angeles (LA) Basin flights in grey). The panel a) show the NO_y budget in smoke plumes, while the panel b) shows that in background air. C₁-C₅ alkyl nitrates are referred to as C₁-C₅ ANs. Other nitrogen species include N_2O_5 , CH_3NO_2 , and alkene hydroxy nitrates.

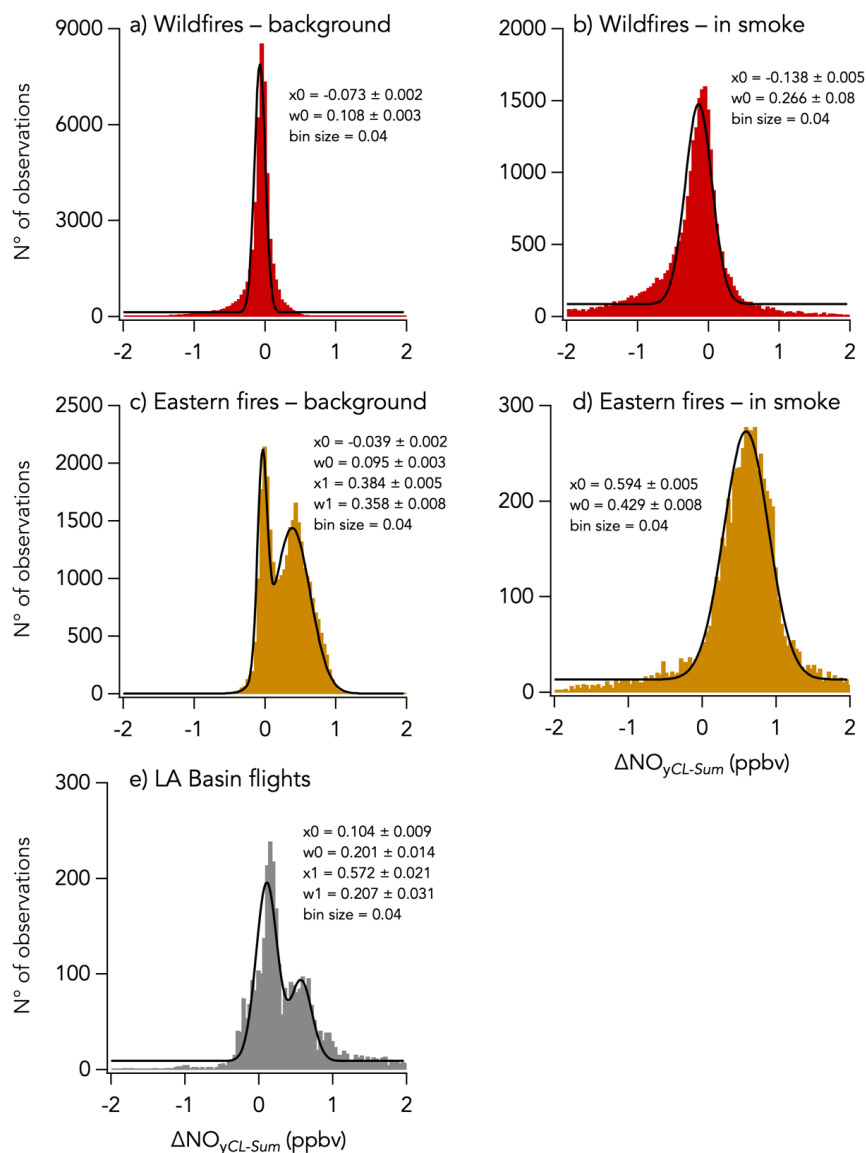


Figure 11 Histograms of $\Delta\text{NO}_{y\text{CL-Sum}}$ for three sampling periods during FIREX-AQ with the wildfires sampling period in red, the eastern fires sampling period in yellow, and the Los Angeles (LA) Basin flights in grey. Further separation was made between in smoke measurements (panels b and d) and background air measurements (panels a, c, and e). Parameters of the gaussian fit to the histogram is indicated in each panel with x_0 and w_0 being the central value and the width of the fit, respectively. Note that in the panels c) and e) a double gaussian was fitted to the histogram and that the parameters for the second mode are given by x_1 and w_1 .

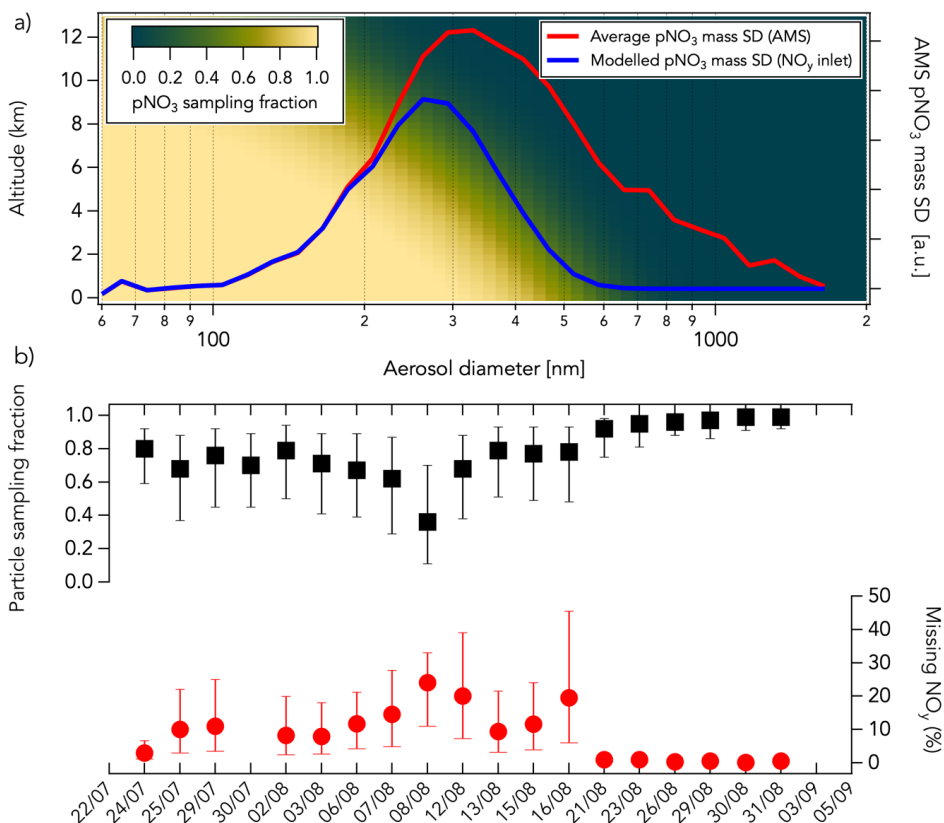


Figure 12 Panel a): The modelled pNO₃ sampling fraction through the NO_y inlet as a function of altitude and pNO₃ mass size distribution (SD) is shown with a gradient of color from green (low sampling fraction) to yellow (high sampling fraction). The average pNO₃ mass size distribution measured in the Williams Flat fire smoke on 07/08/2019 by HR-AMS is shown in red. The modelled pNO₃ size distribution sampled in the NO_y inlet assuming an altitude of 5km and a sampled air speed 65% that of the aircraft is shown in blue. In this example case, the sampled pNO₃ mass fraction is ~50%. Panel b): The average modelled particle sampling fraction in the NO_y inlet (in black) and the corresponding percentage of measured NO_y that may be unaccounted for (in red) are shown for each flight assuming a sampled air speed of 40% (bottom bars), 65% (markers) and 100% (top bars) that of the aircraft speed. The sampling fractions were calculated using bulk aerosol volume distributions measured by a Laser Aerosol Spectrometer (see Section S1 and Figure SC). The missing NO_y corresponds here to the percentage of measured NO_y that pNO₃ not sampled through the NO_y inlet represents. Data shown in the panel b) are from air in smoke only.

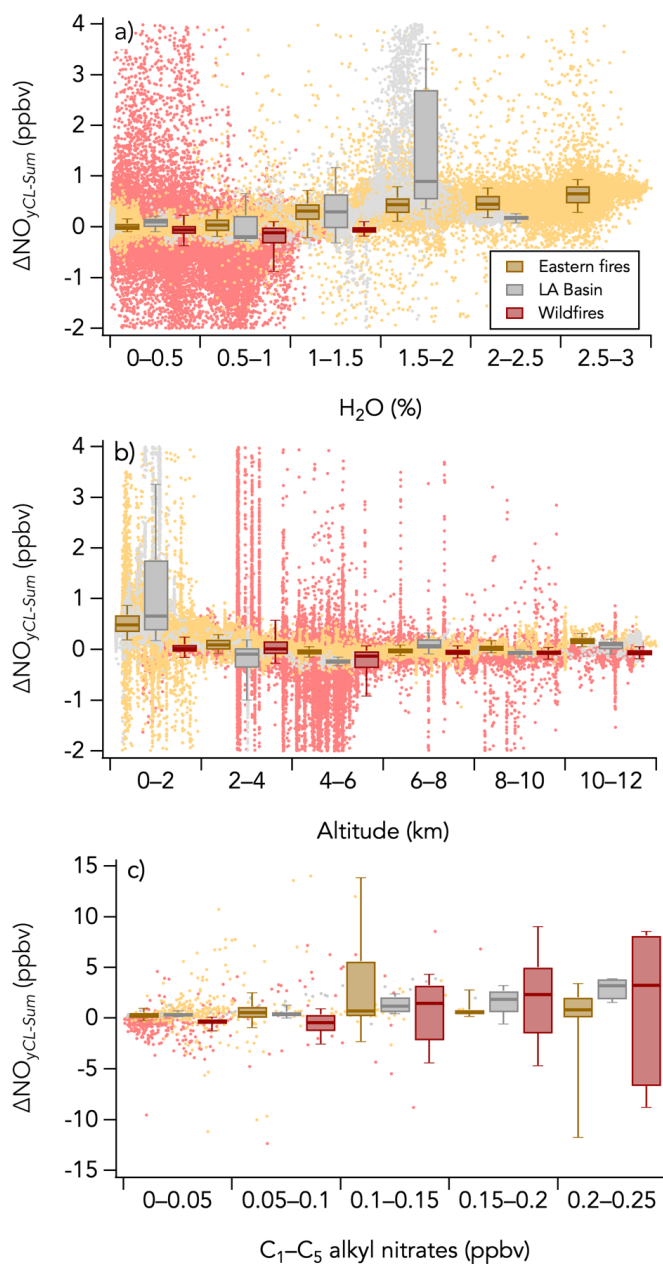


Figure 13 Scatterplots of a) $\Delta\text{NO}_{y\text{CL-Sum}}$ vs H_2O , b) $\Delta\text{NO}_{y\text{CL-Sum}}$ vs altitude and c) $\Delta\text{NO}_{y\text{CL-Sum}}$ vs $\text{C}_1\text{-C}_5$ alkyl nitrates measured by the iWAS instrument for three sampling periods during FIREX-AQ (wildfires sampling period in red, eastern fires sampling period in yellow, and Los Angeles (LA) Basin flights in grey). The box and whisker plots show the 10th, 25th, 50th, 75th, and 90th percentiles of $\Delta\text{NO}_{y\text{CL-Sum}}$ distributions in each bin. The dots are the 1Hz data in panels a) and b), and 1Hz data averaged to match the iWAS sampling time in panel c).

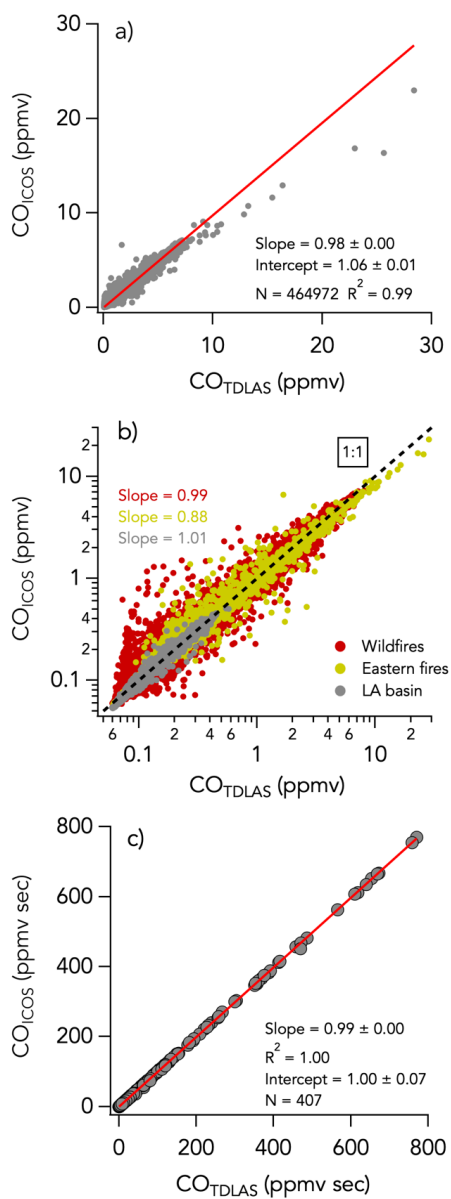


Figure 14 Same as Figure 2 but comparing CO measurements by TDLAS and ICOS.